Uncovering the association mechanism between two intrinsically flexible proteins

Angy L.Dávalos,[†] José D. Rivera,[†] Denize C. Favaro,[‡,§] Ronaldo J. Oliveira,[¶] Gustavo PB. Carretero,[†] Caroline D. Lacerda,[†] Iolanda M. Cuccovia,[†] Marcus V. C. Cardoso,[†,‖] Chuck S. Farah,[†] and Roberto K. Salinas[*,†]

†*Department of Biochemistry, Institute of chemistry, University of São Paulo, São Paulo, Brazil.*

‡*Department of Organic Chemistry, State University of Campinas, Campinas, Brazil*

¶*Department of Physics, Institute of Exact, Natural and Educational Sciences, Federal University of Triângulo Mineiro, Uberaba, Brazil.*

§*Structural Biology Initiative, CUNY Advanced Science Research Center, New York, NY.*

‖*Current address: Department of Chemistry, Institute of Exact and Biological Sciences, Federal University of Ouro Preto, Ouro Preto, Brazil.*

E-mail: roberto@iq.usp.br

Abstract

The understanding of protein-protein interaction mechanisms is key to the atomistic description of cell signalling pathways and for the development of new drugs. In this context, the mechanism of intrinsically disordered proteins folding upon binding has attracted attention. The VirB9 C-terminal domain ($VirB9^{Ct}$) and the VirB7 N-terminal motif ($VirB7^{Nt}$) associate with VirB10 to form the outer membrane core complex of the Type IV Secretion System injectisome. Despite forming a stable and rigid complex, $VirB7^{Nt}$ behaves as a random coil while $VirB9^{Ct}$ is intrinsically dynamic

in the free state. Here we combined NMR, stopped-flow fluorescence and computer simulations using structure-based models to characterize the VirB9^{Ct}-VirB7^{Nt} coupled folding and binding mechanism. Our data indicated that VirB9^{Ct} binds to VirB7^{Nt} by way of a conformational selection mechanism. However, at higher temperatures energy barriers between different VirB9^{Ct} conformations are more easily surpassed. Under these conditions the formation of non-native initial encounter complexes may not be neglected, providing alternative pathways towards the native complex conformation. These observations highlight the intimate relationship between folding and binding, calling attention to the fact that the two molecular partners must search for the most favored intramolecular and intermolecular interactions on a rugged and funnelled conformational energy landscape, along which multiple intermediates may lead to the final native state.

Introduction

Intrinsically disordered proteins (IDPs) are fully functional despite lacking a defined folded structure. When combined with folded domains, they are called intrinsically disordered regions (IDRs).[1–4] IDPs/IDRs may be classified as molecular recognition features (MoRFs), short linear motifs (SLiMs) or low-complexity regions (LCRs).[5] While fuzzy complexes that retain a high degree of disorder in the bound state have been described,[6–9] most MoRFs become structured upon binding to well-folded partners.

The understanding of protein-protein interaction mechanisms is key to the atomic level description of cell signalling pathways and for the development of new drugs. In this context, the mechanism of IDPs/IDRs folding upon binding is of significant interest.[7,9–15] The induced-fit and conformational selection mechanisms have been widely used to explain protein-ligand interactions.[16–18] In the context of IDPs/IDRs, the conformational selection mechanism requires unfolded and folded or partially folded conformations to be in equilibrium with each other, with one of them being the binding competent conformation. In

contrast, the induced fit mechanism requires that folding occurs after binding. Folding and binding have been considered as analogous processes, which may be interpreted in the framework of folding funnels.[18–20] The rugged conformational energy landscape of IDPs/IDRs binding equilibrium could provide multiple pathways for the system to progress downhill towards the native complex. Consistent with this view, it was predicted that induced-fit and conformational selection could co-exist, and the relative importance of one or the other mechanism could be regulated by the ligand concentration.[21] Indeed, complex mixtures of induced-fit and conformational selection have been described.[4,7,9,10,22] In addition, the formation of productive initial encounter complexes between IDPs and folded proteins have been observed by NMR.[23,24] Therefore, folding coupled to binding seems to be a highly cooperative process with few short-lived intermediates, resembling the folding of globular proteins.[25]

Bacteria use secretion systems or injectisomes to transport macromolecules, such as proteins or DNA, across the bacterial cell envelope and to inject them into another prokaryotic or eukaryotic cell.[26] Among them, the Type IV Secretion System from the phytopathogen *Xanthomonas citri* (X-T4SS) is specialized in the secretion of toxins that kill other Gram-negative bacteria.[27] The X-T4SS is part of the warfare arsenal that enables *X. citri* to compete for space and resources with other bacteria.[27,28] Structural characterization of the X-T4SS outer membrane core complex (OMCC) showed a tetradecameric ring formed by multiple copies of VirB7, VirB9 and VirB10. This large assembly spans the bacterial periplasm, making a pore in the outer membrane.[28] The VirB7-VirB9 interaction is stabilized by the binding of VirB7 N-terminal tail ($VirB7^{Nt}$) to the VirB9 C-terminal domain ($VirB9^{Ct}$). This $VirB7^{Nt}$-$VirB9^{Ct}$ complex consists of a sandwich of two antiparallel β sheets, one of them formed by four $VirB9^{Ct}$ β-strands, and another formed by a short VirB7 β-strand that pairs with VirB9 $\beta1$, forming the $\beta0$-$\beta1$-$\beta8$-$\beta7$-$\beta4$ β-sheet **(Figure 1)**.[28,29] The $VirB7^{Nt}$ - $VirB9^{Ct}$ interaction was shown to be critical for OMCC stabilization and X-T4SS functioning.[29]

NMR data indicated that $VirB7^{Nt}$ is intrinsically disordered in the absence of $VirB9^{Ct}$,

while the latter is highly flexible, presumably a molten globule, in the free state.[29,30] Considering their intrinsic dynamic nature, VirB9^{Ct} and VirB7^{Nt} form an ideal model system to study the mechanism of coupled folding and binding between two intrinsically flexible proteins. To this end, we characterized the VirB7^{Nt}-VirB9^{Ct} binding mechanism using a combination of ^{15}N chemical exchange saturation transfer (CEST) experiments, stopped-flow fluorescence and computer simulations using classical and structure-based models.

Results and Discussion

Structural characterization of VirB9^{Ct} in the unbound state

The circular dichroism (CD) spectrum of VirB9^{Ct} in aqueous solution showed a negative band at 218 nm indicative of β type structures **(Figure 2A)**.[31] A quantitative analysis of this spectrum indicated that approximately 39 VirB9^{Ct} residues (37%) are in β type conformation. The NMR structure of the VirB7^{Nt}-VirB9^{Ct} complex (PDB 2N01) showed a slightly larger number of residues, 46 VirB9^{Ct} residues (44%), in β-type conformation.[29] The positive CD band at 232-233 nm could be due to the presence of six phenylalanines and one tryptophan in the VirB9^{Ct} amino acid sequence. It is known that aromatic residues may give rise to exciton coupling effects,[32–35] which seem to significantly contribute to the CD spectra of proteins with low helical content.[32] The CD spectrum of VirB7^{Nt} is typical of a random coil, as expected for a short peptide in aqueous solution **(Figure 2A)**. The VirB7^{Nt} peptide is a good model for the N-terminal tail within VirB7, which shows fast backbone motions as revealed by measurements of ^{15}N relaxation rates.[30]

The hydrophobic fluorescent probe 8-anilino-1-naphthalene sulfonic acid (ANS) is a good probe of solvent-exposed hydrophobic surface patches on proteins. Binding of ANS to hydrophobic patches is accompanied by an increase in fluorescence intensity and a shift of the fluorescence spectrum towards shorter wavelengths.[36,37] Addition of VirB7^{Nt} did not affect the ANS fluorescence **(Figure 2B)**. However, the addition of either VirB9^{Ct} alone or in

complex with VirB7^{Nt} resulted in a small but significant increase in the ANS fluorescence accompanied by a blue-shift of the spectrum **(Figure 2B)**. The greater ANS fluorescence change observed upon addition of the free protein relative to the complex indicates that the unbound VirB9^{Ct} exposes a greater amount of hydrophobic surface area than the complex.

The thermal denaturation of VirB9^{Ct} and of the VirB9^{Ct}-VirB7^{Nt} complex was monitored by differential scanning calorimetry ($\mu-$DSC) and CD. A reversible thermal transition was observed at nearly the same melting temperature (T_m) for the unbound VirB9^{Ct} and for the complex by both methods **(Figures 2C and 2D)**. This observation was surprising since binding to VirB7^{Nt} was expected to promote an extra thermal stabilization of VirB9^{Ct}, which should be reflected in a higher T_m relative to the unbound protein.[38–41] Notably, the thermal denaturation experiment showed that the complex has significantly higher unfolding enthalpy (29.57 kcal/mol) than the unbound VirB9^{Ct} (10.42 kcal/mol) **(Figure 2C)**. This observation may be explained considering that VirB9^{Ct}-VirB7^{Nt} unfolding and dissociation occur within a single transition as a consequence of the coupling between these two processes.[42–44]

The magnitude of the heat capacity change upon binding (ΔC_p) is strongly correlated to the amount of solvent-exposed surface area that is buried upon complex.[45–47] Binding of VirB9^{Ct} to VirB7^{Nt} is enthalpically driven as indicated by isothermal titration calorimetry (ITC) experiments carried out at 10, 25, and 35 °C **(Figure 3A and B)**. The VirB9^{Ct}-VirB7^{Nt} K_d^{app} is 0.7 μM at 35 °C, similar to the value reported before.[29] Analysis of the binding ΔH temperature dependence revealed a $\Delta C_p = -0.23 kcal/(K \times mol)$ **(Figure 3C)**, which is a small value consistent with an interaction with minor conformational rearrangements.[47–49] As an example, binding of the HIV-1 envelope glycoprotein gp120 to the human cell surface CD4 receptor involves substantial structuring coupled to binding, which is reflected on a large $\Delta C_p = -1.3 kcal/mol \times K$.[49] In contrast, binding of MAb b12 to gp120 does not induce any conformational structuring and leads to a reduced $\Delta C_p = -0.4 kcal/mol \times K$.[49]

We used solution NMR spectroscopy to characterize the structure of VirB9^{Ct} in the unbound state. The ^{1}H-^{15}N HSQC spectrum of the unbound protein showed a lower number of

cross-peaks than expected based on the amino acid sequence, and a pronounced temperature dependence. Specifically, line width sharpening was observed as the temperature decreased from 35 to 7 °C (not shown). From the 100 ^{1}H-^{15}N cross peaks expected based on the VirB9^{Ct} amino acid sequence, approximately 92 were detected at 7 °C. We successfully assigned 70 of them from the analysis of a set of multidimensional triple resonance NMR experiments recorded at the lowest possible temperature **(Figure 4A)**. The unassigned residues were mainly located within β-strands β1 and β2, which form the VirB7^{Nt} binding site **(Figure 1)**. Secondary structure prediction based on the assigned chemical shifts using TALOS[50] indicated that β strands β_3 to β_8 were already folded in the unbound state, as well as the short 3_{10}-helix in the β_3-β_4 inter-strand loop **(Figure 4B)**. Curiously, an additional short α-helix was detected in the β_4-β_5 inter-strand loop **(Figure 4B)**. This extra helix is absent in the structure of the bound state, however the NMR structure of the complex was solved at a significantly higher temperature, 35 °C **(Figure 1)**.

To obtain additional chemical shift information for the unbound VirB9^{ct}, particularly along β-strands β1 and β2, we performed chemical exchange saturation transfer (CEST) experiments of ^{15}N labeled VirB9^{Ct} in the presence of sub-stoichiometric concentrations of unlabeled VirB7^{Nt}. This ^{15}N-CEST experiment was recorded at 35 °C instead of 7 °C because the exchange between unbound and bound VirB9^{Ct} was not observed at lower temperatures **(Supplementary Figure S1)**. This observation is probably a consequence of the increased affinity between VirB9^{Ct} and VirB7^{Nt} at low temperatures **(Figure 3)**. Analysis of the ^{15}N-CEST experiment showed that some of the VirB9^{Ct} residues presented two ^{15}N-CEST dips as exemplified by F237 in β7 **(Figure 5A)**, revealing a two-states chemical exchange process, while others, exemplified by D244 in the β7-β8 inter-strand loop, showed only a single ^{15}N-CEST dip and no evidence of chemical exchange at all **(Figure 5B)**. Furthermore, a subset of residues such as R172 in the β1-β2 inter-strand loop, displayed three ^{15}N-CEST dips reveling a three-states exchange process **(Figure 5C)**. Further addition of VirB7^{Nt} caused a decrease in the magnitude of the smaller dips, corroborating their assignment to unbound VirB9^{Ct}

species in slow exchange with the major VirB7$^{\mathrm{Nt}}$-bound state **(Figures 5A and 5C)**. All VirB9$^{\mathrm{Ct}}$ residues that showed exchange between the unbound and the VirB7$^{\mathrm{Nt}}$-bound states were located within β-strands β1 and β2 or within the β1-β7-β8-β4 antiparallel β-sheet over which VirB7$^{\mathrm{Nt}}$ lies on **(residues colored red and green in Figure 5D)**. The single exception is T223 in β5. The ^{15}N-CEST profiles displaying two-states exchange were fitted to the Bloch-McConnell equation assuming a two-states exchange model **(Supplementary Figure S2)**. The fitted exchange rate was $k_{\mathrm{ex}}^{\mathrm{b}} \approx$ 15-20 s^{-1}, with the unbound state population $p_{\mathrm{A}} \approx$ 7 - 10% of the total VirB9$^{\mathrm{Ct}}$ population. Backbone ^{15}N chemical shifts for residues located within VirB9$^{\mathrm{Ct}}$ β1 and β2 in the unbound state were obtained from the analysis of the ^{15}N-CEST experiment. The backbone ^{15}N chemical shifts for residues 163 - 171 along the β1 showed a very good agreement with random coil chemical shifts predicted from the VirB9$^{\mathrm{Ct}}$ amino acid sequence, while a poorer agreement was observed along β2 **(Figure 6 A and B)**, suggesting that the VirB9^{Ct} β1 is disordered in the absence of VirB7$^{\mathrm{Nt}}$. The relative instability of β1 is supported by molecular dynamics (MD) simulations of VirB9$^{\mathrm{Ct}}$ in the unbound and in the VirB7$^{\mathrm{Nt}}$-bound states **(Supplementary Figures S3 and S4)**. The simulations showed that β1 unfolded after approximately 300 ns in the absence of VirB7$^{\mathrm{Nt}}$, after which the corresponding region exchanged between disordered and helical conformations **(Figure 6-C and Supplementary Figure S2)**. In contrast, the same β-strand remained stable during the whole MD trajectory of the VirB7$^{\mathrm{Nt}}$-bound state **(Figure 6-D and Supplementary Figure S2)**.

Altogether we may conclude that the unbound VirB9$^{\mathrm{Ct}}$ is almost fully folded except for β1, which is disordered. Folding of a small β-strand rather than a larger conformational change is supported by the observation of a relatively small ΔC_p due to VirB7$^{\mathrm{Nt}}$-binding **(Figure 3)**, and by the CD spectrum that was consistent with all but one β-strand already folded in the unbound state **(Figure 2)**.

VirB9^{Ct} samples the bound conformation in the absence of VirB7^{Nt}

Analysis of the ^{15}N-CEST experiment indicated that VirB9^{Ct} assumed at least two unbound conformations in slow exchange equilibrium with the VirB7^{Nt}-bound state **(Figure 5)**. As an attempt to test whether VirB7^{Nt} would bind to one of the unbound VirB9^{Ct} conformations rather than the other, we added a larger amount of VirB7^{Nt} to the sub-stoichiometric VirB9^{Ct}-VirB7^{Nt} sample, and repeated the ^{15}N-CEST experiment. We observed a decrease in the magnitude of all CEST dips assigned to the unbound VirB9^{Ct} conformations **(Figure 5C)**, indicating that VirB7^{Nt} displays no preference towards a specific unbound VirB9^{Ct} conformation or that the preferential binding to one of them rapidly shifts the equilibrium between the unbound conformations leading to a concomitant reduction in their populations.

We then investigated whether VirB9^{Ct} could sample the bound conformation in the unbound state. To test this hypothesis, we compared ^{15}N CEST experiments recorded in the absence and presence of sub-stoichiometric VirB7^{Nt} concentrations at 35°C **(Figure 7A and 7C)**. Partial assignments for the unbound VirB9^{Ct} ^{1}H-^{15}N HSQC spectrum at 35 °C were obtained from the analysis of a ^{15}N$_z$-exchange experiment and a series of HSQC experiments recorded at increasing temperatures from 7 to 35 °C **(Supplementary Figure S5)**. Some of the VirB9^{Ct} residues exhibited a broad and rather noisy ^{15}N-CEST profile in the unbound state as shown for L178, while others exhibited well separated ^{15}N-CEST dips, indicating their engagement in the slow exchange equilibrium between distinct conformations as shown for R172 in the β1-β2 inter-strand loop **(Figures 7A and B)**. These observations revealed the dynamic regions of the unbound VirB9^{Ct} **(colored magenta in Figure 7B)**. Other residues, such as F189 and H214, showed a single CEST dip indicating that they were located in rigid parts of the unbound VirB9^{Ct} **(colored black in Figures 7A and 7B)**. The ^{15}N-CEST profiles for all residues located in the dynamic regions of the unbound state showed a drastic change upon the addition of VirB7^{Nt}. Specifically, CEST dips corresponding to unbound conformations sharpened, giving rise to a major CEST dip at the bound state ^{15}N chemical shift as exemplified for R172 and L178 in the β1-β2 inter-strand loop **(Figure 7C)**.

These VirB9^{Ct} residues **(colored green in Figure 7D)** experience multiple conformations in the unbound state, one of them corresponding to the VirB7^{Nt}-bound conformation, which suggest that VirB9^{Ct} may bind to VirB7^{Nt} according to a conformational selection mechanism. Residues located in the rigid parts of the unbound VirB9^{Ct}, such as H214 and F189, exhibited a new ^{15}N CEST dip corresponding to the VirB7^{Nt}-bound state (H214) or experienced no change at all (F189) **(Figure 7C and 7D)**. The latter cases, exemplified by F189, correspond to residues located far away from VirB7^{Nt} binding site, explaining why they do not experience significant chemical shift changes upon Vir7^{Nt} binding. The former cases, exemplified by H214, correspond to residues that experienced a significant ^{15}N chemical shift change upon binding **(Figure 7D)**. Such chemical shift changes could be explained by the proximity to VirB7^{Nt} rather than a VirB9^{Ct} conformational change **(Figure 7D and E)**.

The VirB9^{Ct}-VirB7^{Nt} binding mechanism

The presence of tryptophan residues at positions 177 and 34 in VirB9^{Ct} and VirB7^{Nt}, respectively, and the millisecond exchange time scale between unbound and bound VirB9^{Ct} states, favored the use of stopped-flow fluorescence to follow VirB9^{Ct}-VirB7^{Nt} association kinetics. At 25°C and under pseudo first order conditions for VirB7^{Nt} (varying [VirB7^{Nt}] and keeping [VirB9^{Ct}] constant), the experimental traces were found to be bi-exponential **(Supplementary Figure S6, A and B)**, indicating the occurrence of two events as expected for a coupled folding and binding process.[7,22,51,52] The faster and the slower kinetic rate constants (k^1_{obs} and k^2_{obs}) increased as a function of the ligand concentration (VirB7^{Nt}), which is consistent with both the conformational-selection (CS) and the induced-fit (IF) mechanisms[51–53] **(Figure 8A and B)**. The ambiguity between these two mechanisms was resolved by performing the same kinetic experiment under reverse pseudo-first order conditions, i.e varying the concentration of VirB9^{Ct} while keeping [VirB7^{Nt}] constant.[22,51,54] The reverse pseudo-first order experiment carried out at 25°C yielded mono-exponential kinetic traces **(Supplementary Figure S6,C and D)**, suggestive of a single step. The observed kinetic

rate constant was shown to increase linearly with the VirB9^{Ct} concentration, in agreement with the binding event **(Figure 8C)**. These observations suggest that the VirB9^{Ct} interaction with VirB7^{Nt} is governed by a conformational-selection mechanism at 25°C.[51,53,54] Notably, when the kinetic experiments were repeated at 35 °C, the faster kinetic rate constant (k^1_{obs}) increased linearly with the VirB7^{Nt} concentration, while the slower kinetic rate constant (k^2_{obs}) decreased hyperbolically as a function of [VirB7^{Nt}] **(Figure 8D)**. The decreasing behavior of k^2_{obs} as a function of the free VirB7^{Nt} concentration is a kinetic signature of the conformational-selection mechanism **(Figure 8D)**.[51,53] However, when the kinetic experiments were repeated under reverse pseudo-first order conditions, the experimental traces were bi-phasic **(Supplementary Figure S7, C and D)** in contrast to what was observed at 25°C **(compare figures 8C and 8E)**. Under these conditions, the fast and the slow kinetic rate constants, k^1_{obs} and k^2_{obs}, increased linearly and hyperbolically with the VirB9^{Ct} concentration, respectively **(Figure 8E)**. The hyperbolic behavior of k^2_{obs} is consistent with both the IF and the CS mechanisms.[53] We propose that the hyperbolic increase of k^2_{obs} as a function of the [VirB9^{Ct}] **(Figure 8E)** corresponds to a third event distinct from both VirB9^{Ct} conformational exchange or the binding to VirB7^{Nt}. This third event could be a conformational rearrangement of the complex after binding, i.e. an IF event that is observed only at the higher 35 °C temperature **(Figure 8E)**. It is unclear why this third event was not observed under conditions of excess of VirB7^{Nt} **(Figure 8D)**. One possible explanation is that such IF event takes place at a timescale closer to k^1_{obs}, resulting in a contaminated kinetic rate constant as suggested by its distorted behavior moving away from the linearity **(Figures 8D, E and 8F)**.

The kinetic data obtained at 25 °C under conditions of excess of VirB7^{Nt} was fitted to a CS kinetic model **(Scheme 1)**. This model assumes that, in the unbound state, VirB9^{Ct} undergoes an equilibrium between two conformations, P and P*, where P corresponds to the bound-like or native VirB9^{Ct} conformation, and P* is the non-native VirB9^{Ct} conformation. The VirB9^{Ct} conformational exchange rate constants, k_A and k_B, as well as the association

constants k_{on} and k_{off} **(Scheme 1)**, were considered as free parameters. The VirB9^{Ct}-VirB7^{Nt} K_d^{int} determined in this experiment was approximately 0.2 μM, in the same order of magnitude as the apparent K_d^{app} determined by ITC **(Table 2)**.

The kinetic data obtained at 35 °C were fitted to a three sequential events model due to the observation of three kinetic phases **(Scheme 2 and Supplementary Figure S8)**. This model combines the CS and IF mechanisms, where k_A, k_B, k_C and k_D define the forward and reverse conformational exchange rate constants between the VirB9^{Ct} P* and P conformations, and between an initial encounter complex and the final native-like complex, designated C* and C, respectively. The association rate constants k_{on} and k_{off} would be related to the binding of VirB7^{Nt} to VirB9^{Ct} in the non-native P* conformation forming an initial encounter complex denoted C*. The fitted parameters showed that k_{on} is nearly constant at 35 and 25°C **(Table 1)**, which is consistent with the nearly parallel behavior of k_{obs}^1 as a function of [VirB9^{Ct}] at 25 and 35°C **(Figure 8-G)**. In contrast, k_{off} increased from ≈ 0.42 s^{-1} at 25°C to 3.06 s^{-1} at 35°C, explaining the higher K_d at 35°C compared to 25°C **(Tables 1 and 2)**. The lower k_{off} at 25 °C is consistent with the observed absence of chemical exchange between unbound and bound VirB9^{Ct} when the CEST experiments were recorded at similar temperatures **(Supplementary Figure S1)**. Notably, the calculated rate constants associated with the VirB9^{Ct} conformational transitions (k_A and k_B), reflect a change in the equilibrium between native (P) and non-native (P*) VirB9^{Ct} conformations as a function of temperature. This conclusion is supported by temperature-dependence of the equilibrium constant between P* and P, given by k_A/k_B, which changed from $K_{eq}^{\mathbf{P^*}\rightarrow\mathbf{P}} = 15.0$ at 25 °C to $K_{eq}^{\mathbf{P^*}\rightarrow\mathbf{P}} = 3$ at 35 °C **(Table 1 and Figure 9-Bottom)**. This VirB9^{Ct} conformational ensemble redistribution at 35 °C is in agreement with the large temperature dependence of the VirB9^{Ct} NMR spectrum **(Figure 4 and supplementary figure S5)**.

In summary, while the kinetic data obtained at 25 °C is consistent with a conformational selection binding mechanism, at 35 °C the greater populations of distinct VirB9^{Ct} conformations must increase the probability of additional binding pathways, in which the formation

of initial non-native encounter complexes is followed by conformational rearrangements towards the native complex **(Figure 9-Top)**. These two binding pathways might compete with each other for the formation of the final complex. The predominance of one or the other binding pathway seems to be determined by the temperature-dependent balance of the VirB9^{Ct} conformational equilibrium **(Figure 9-Bottom)**.

Computer simulation of the free energy landscape of the VirB9^{Ct}-VirB7^{Nt} coupled folding and binding process

Simulations of the structure-based model (SBM)[55] in all-atom representation of the VirB9^{Ct}-VirB7^{Nt} complex were executed in a wide range of temperatures that sampled binding and folding of the protein and peptide chains. Configurational search was enhanced with simulations at temperatures close to the VirB9^{Ct}-VirB7^{Nt} binding temperature (T_{bind}), where binding/unbinding events had roughly equal probabilities to occur. The many long-run simulations sampled the complex configurational space and were analyzed by the thermodynamic WHAM algorithm.[56] **Figure 10** shows the resulting thermodynamic Helmholtz free energy surface (F) of the VirB9^{Ct}-VirB7^{Nt} recognition process. F is displayed along two reaction coordinates that count the number of native contacts: the intramolecular folding of VirB9^{Ct} (Q_{fold}) and the intermolecular binding contacts between VirB9^{Ct} and VirB7^{Nt} (Q_{bind}). At T_{bind}, the simulated system displayed three stable free energy minima and one metastable state **(Figure 10)**. Two of them correspond to the unbound VirB9^{Ct} state, and were indicated as P and P* in analogy with the intermediate states highlighted by the stopped flow fluorescence data. Following the same analogy, the metastable and the stable bound-state free energy basins were depicted C* and C, respectively **(Figure 10)**. **Figure 10B** shows an illustrative time trajectory of the complex projected over F with representative structures of the three F minima (P*, P and C) and of the meta-stable C* state. The time trajectory window is also plotted in **Figure 10C**. It is noteworthy that complex dissociation leads to a minimum free energy basin along which VirB9^{Ct} is partially folded, indicated by P* in

Figure 10C.

This theoretical experiment showed that starting from the unbound and partially folded P* F basin in **Figure 10B**, there is a small energetic F barrier ($\sim 1k_bT$) along the VirB9^{Ct} folding coordinate to the still unbound but folded P ensemble (between P and P*) **(Figure 10B)**. From there, VirB9^{Ct} is able to bind to VirB7^{Nt} after crossing F barriers of about $9k_bT$ via the C* metastable state or directly to the folded and bound C native state of VirB9^{Ct}-VirB7^{Nt}. It is also possible to concomitantly fold and bind from the P* to the C* and then C or directly to C, although the probability is lower (free energy barriers are higher). These are the proposed folding and binding mechanisms of VirB9^{Ct} and VirB7^{Nt} discussed in the previous sections. It is a direct consequence of the energy landscape theory that accommodates the conformational selection and the induced fit mechanisms over a funneled surface towards the lowest energy basin containing the folded-bound conformation.[57–59]

Conclusions

We showed previously that VirB7^{Nt} behaves as a random coil and that VirB9^{Ct} is intrinsically dynamic in the unbound state.[29] In this work, we combined different biophysical techniques with computer simulations to characterize the VirB9^{Ct}-VirB7^{Nt} coupled folding and binding mechanism. NMR data obtained for VirB9^{Ct} in the unbound state at 35 °C showed strong evidence that $\beta 1$ is unstructured in the absence of VirB7^{Nt}, while other residues also located at the VirB7^{Nt} binding region experience an equilibrium between multiple conformations at the millisecond time scale. NMR and kinetics data supported conformational selection as the VirB7^{Nt}-VirB9^{Ct} binding mechanism. However, at 25 °C VirB9^{Ct} is partially confined in a bound-like conformational space basin, which favors conformational selection as the major binding mode. In contrast, at 35 °C the energy barriers between different VirB9^{Ct} conformations are more easily surpassed, giving rise to different VirB9^{Ct} conformations and, hence to other binding pathways involving the formation of initial encounter complexes that

will eventually rearrange to the final native conformation **(Figure 11)**. Indeed, analysis of the C* complex metastable state snapshots during the molecular dynamics simulations at T_{bind} showed that VirB7^{Nt} may first anchor itself to VirB9^{Ct} by making intermolecular contacts at the surface of the β1-β8-β7-β4 β-sheet prior to β0 formation **(Figure 11)**. The present scenario calls attention to the fact that, similarly to the folding process, coupled folding and binding involves searching for the most favored intramolecular and intermolecular interactions on a rugged and funnelled conformational energy landscape, in which multiple intermediates may lead to the final native state.

Figures and tables

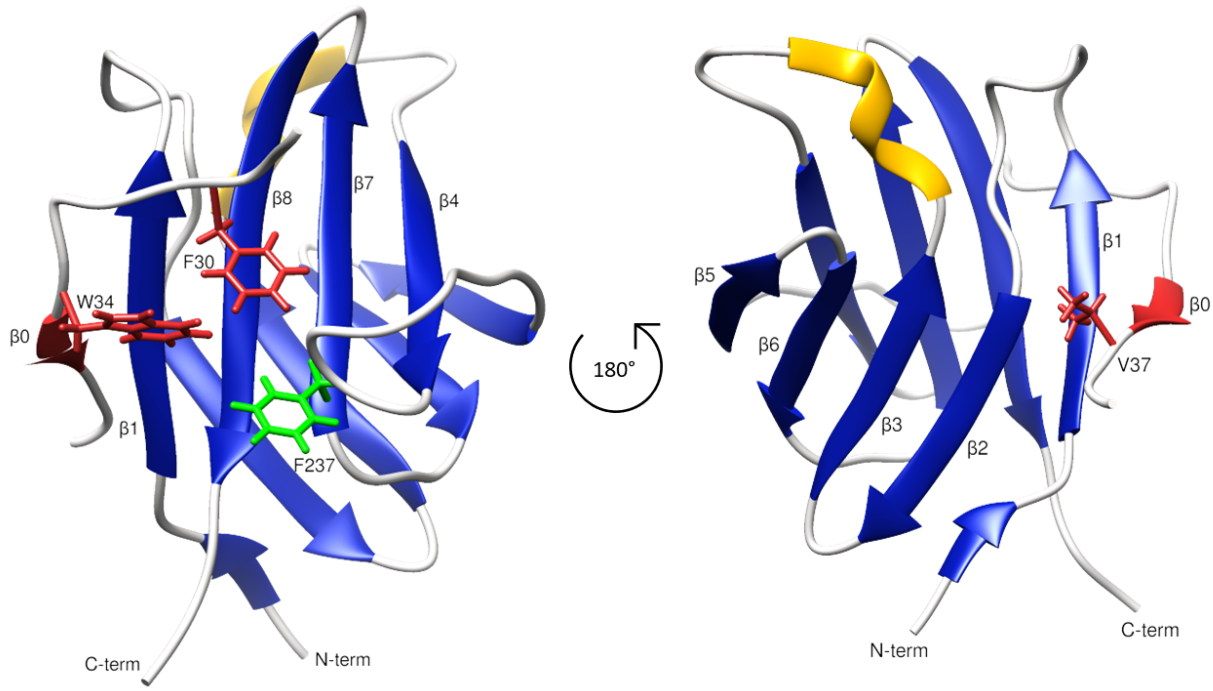

Figure 1: NMR solution structure of the VirB9^{Ct}-VirB7^{Nt} complex (PDB 2N01).[29] The secondary structure is color-coded blue for β-strand and yellow for helix. The VirB7^{Nt} β0 is shown in red. VirB7^{Nt} side chain residues F30 and W34 are shown in sticks and red-colored, while VirB9^{Ct} F237 side chain is shown in green. This complex is stabilized by a series of interactions between VirB7^{Nt} aromatic residues, F30 and W34, and VirB9^{Ct} solvent exposed side chains on the surface of the β1-β8-β7-β4 β-sheet, and by the accommodation of VirB7^{Nt} V37 in a hydrophobic cleft formed between VirB9^{Ct} strands β1 and β2.[29]

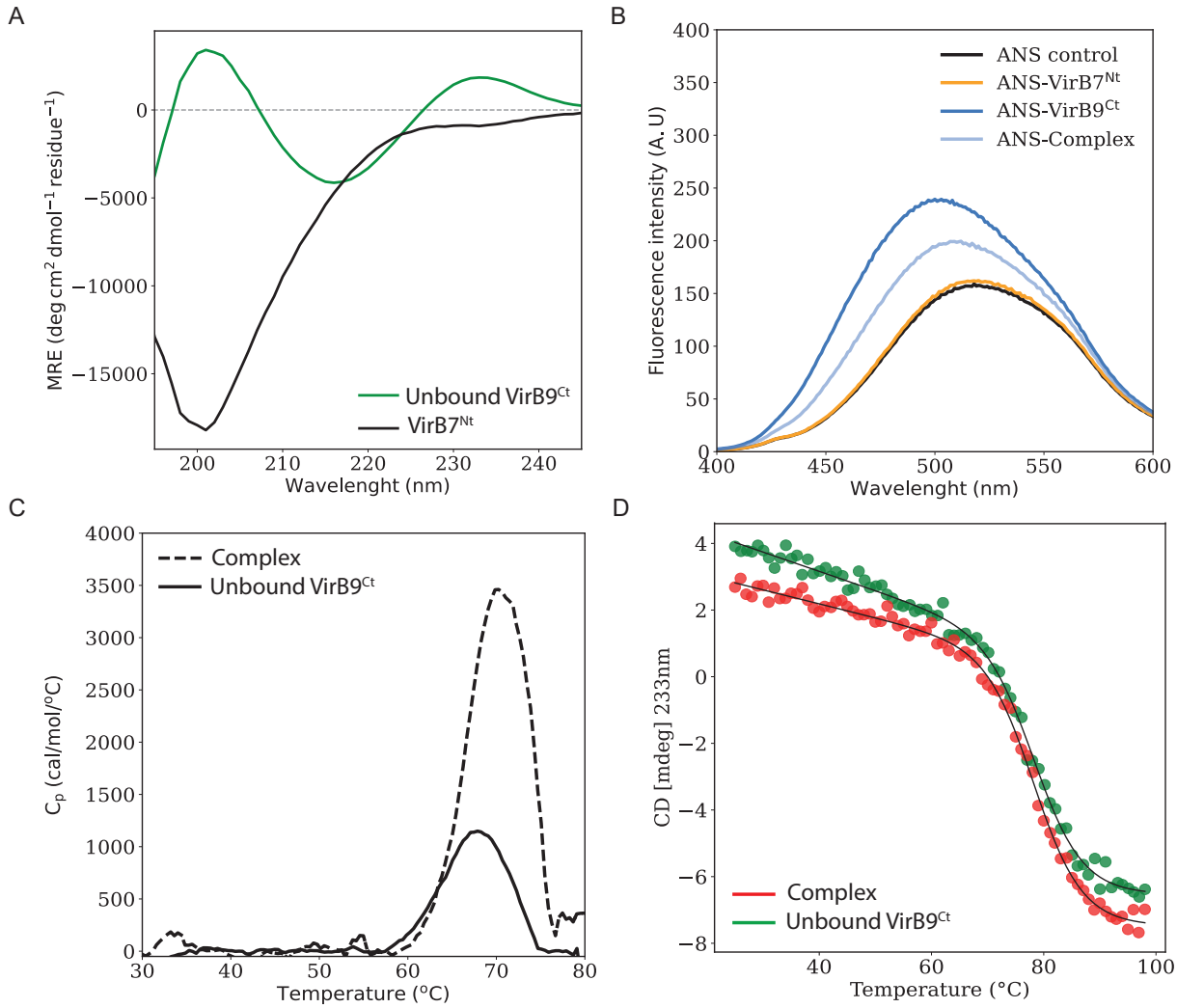

Figure 2: Far-UV CD spectra of the unbound VirB9^{Ct} (green) and VirB7^{Nt} (black) (A). ANS fluorescence spectra recorded in the absence or presence of VirB7^{Nt}, VirB9^{Ct}, and the VirB7^{Nt}-VirB9^{Ct} complex (B). Thermal denaturation of the unbound VirB9^{Ct} and of the VirB7^{Nt}-VirB9^{Ct} complex monitored by DSC (C) or CD at 233 nm (D).

Table 1: Values for the fundamental rate constants obtained from fitting of the stopped-flow kinetic relaxations at 25 and 35°C according to the CS and CS-IF combined model, respectively.

Model	T(°C)	k_A(s^{-1})	k_B(s^{-1})	k_{on}($s^{-1}\mu M^{-1}$)	k_{off}(s^{-1})	k_C(s^{-1})	k_D(s^{-1})
CS-IF	35	≈ 3.42	≈ 1.17	≈ 1.85	≈ 3.06	≈ 1.65	≈ 0.21
CS	25	≈ 6.00	≈ 0.38	≈ 2.08[1]	≈ 0.42		

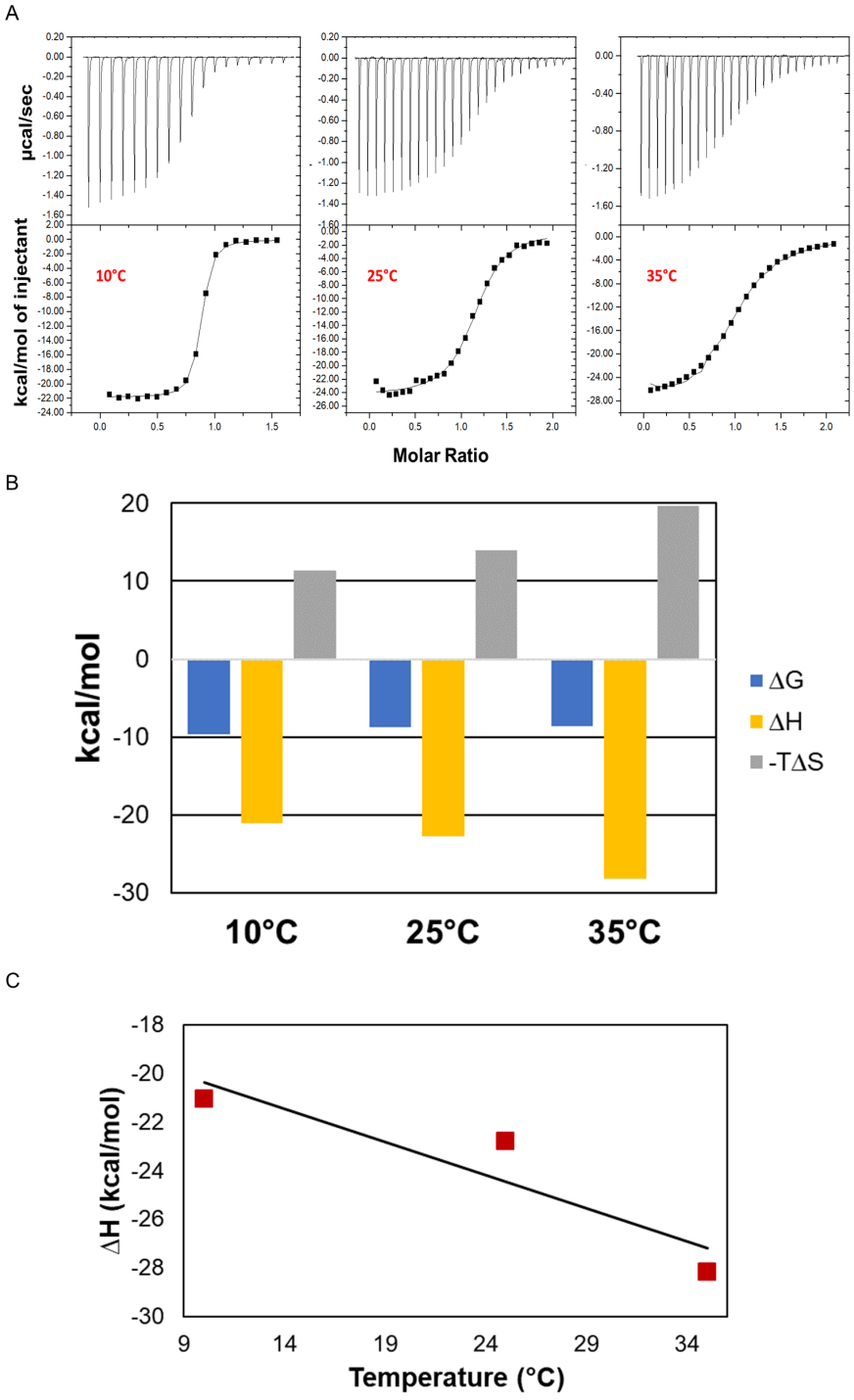

Figure 3: Isothermal titration calorymetry (ITC) thermograms of VirB7$^{\mathrm{Nt}}$ being titrated with VirB9$^{\mathrm{Ct}}$ at 10, 25 and 35°C (A). Values of $\Delta \mathrm{H}^0$, $-T \times \Delta \mathrm{S}^0$ and $\Delta \mathrm{G}^0$ obtained from fitting the ITC data to a 1:1 stoichiometric model (B). ΔC_p (-0.23kcal/mol) obtained from the slope of the graph of $\Delta \mathrm{H}^0$ as a function of temperature (C).

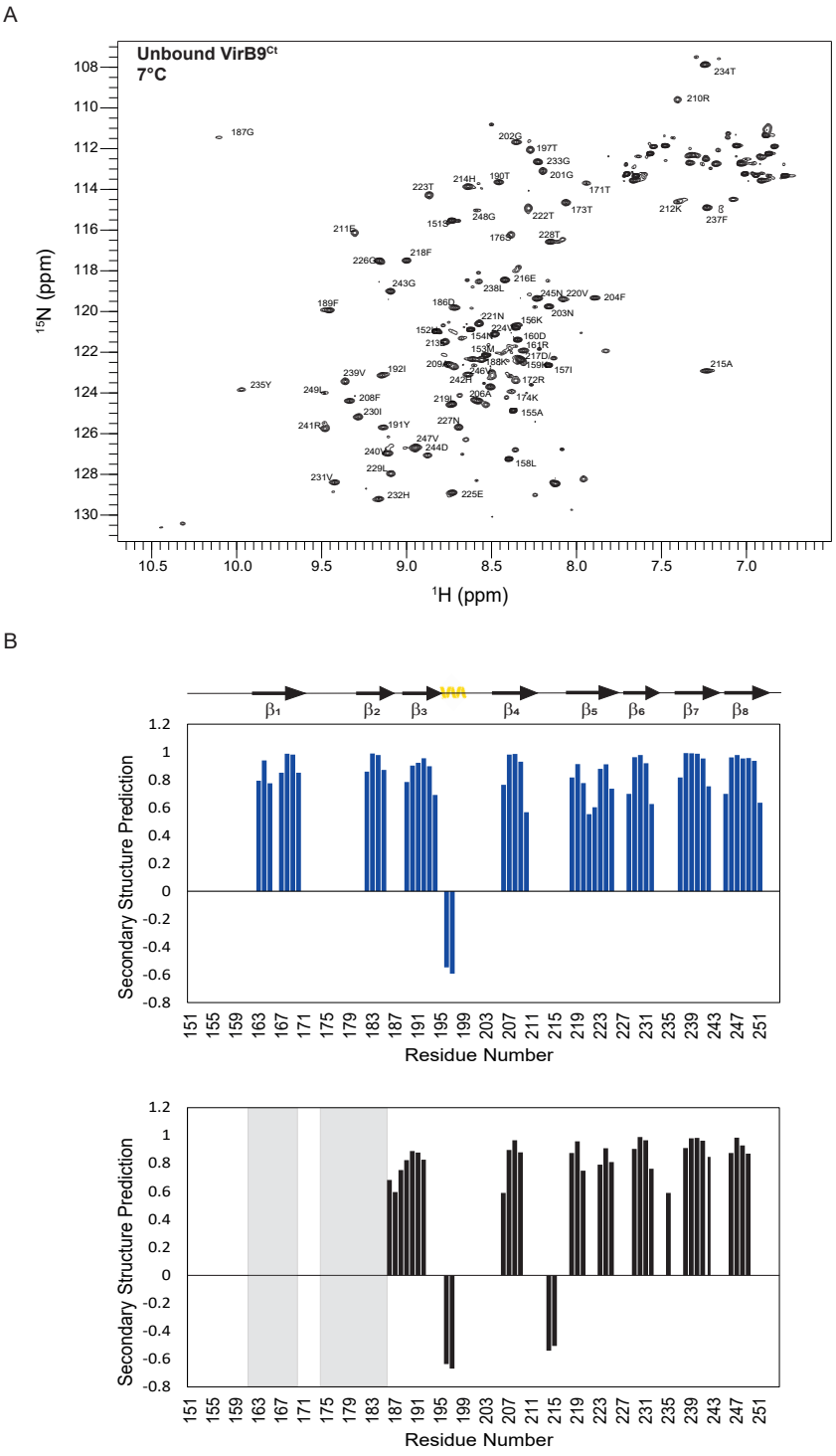

Figure 4: Assignment of the unbound VirB9^{Ct} ^{1}H-^{15}N HSQC spectrum at 7 °C (A). TALOS secondary structure prediction for the bound (blue) and the unbound (black) states of VirB9^{Ct} at 35 and 7 °C, respectively. Unassigned residues are highlighted gray-colored rectangles (B).

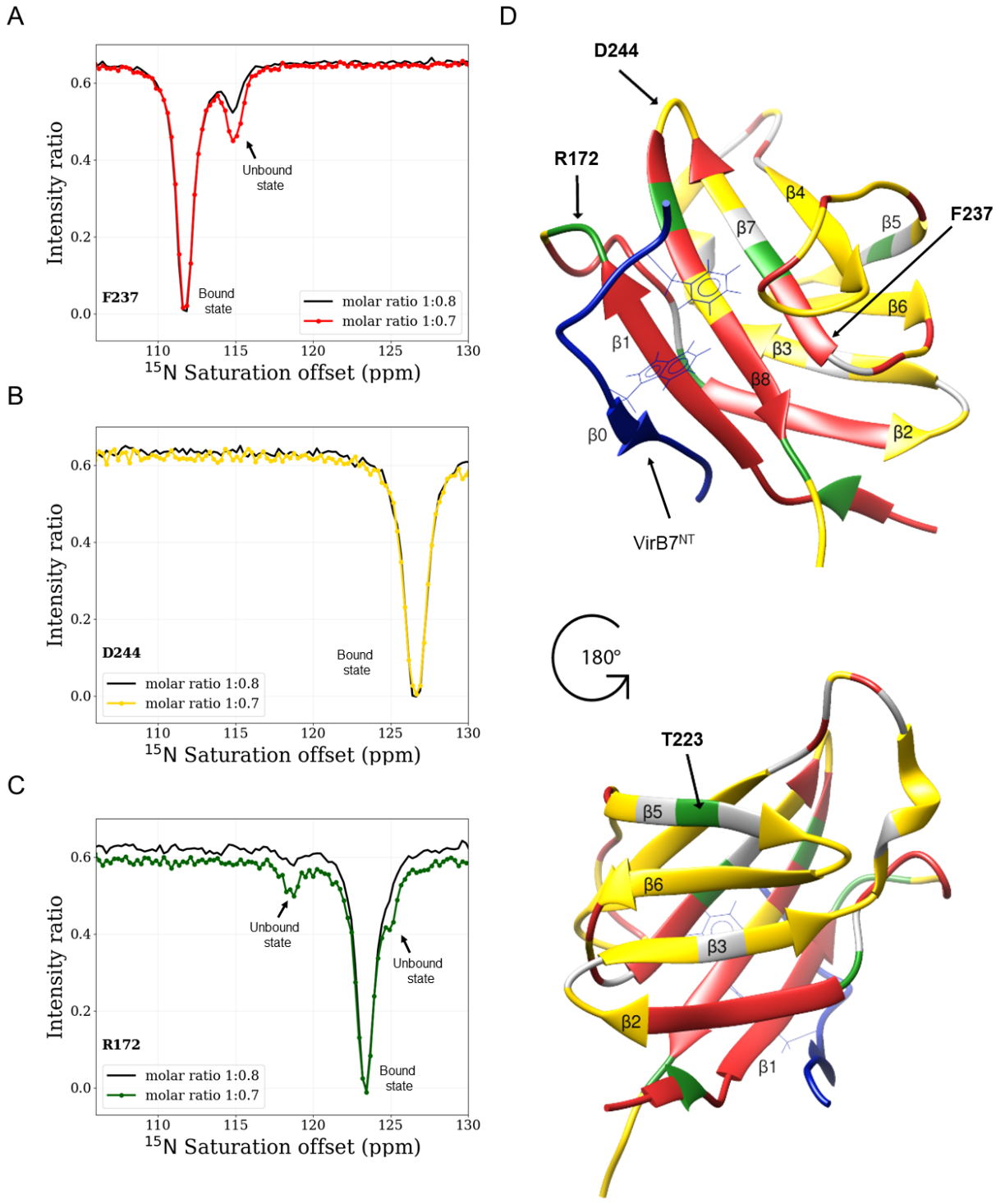

Figure 5: Representative ^{15}N CEST profiles obtained with samples of VirB9^{Ct}-VirB7^{Nt} at approximately 1:0.9 (colored) and 1:0.95 (black) (VirB9^{Ct}:VirB7^{Nt}) molar ratios for residues F237 (A), D244 (B) and R172 (C). VirB9^{Ct} residues displaying ^{15}N-CEST profiles according to A (two CEST dips), B (one CEST dip) and C (three or more CEST dips) are color-coded red, yellow and green, respectively, on the structure of the complex (D). The VirB7^{Nt} peptide is shown in blue.

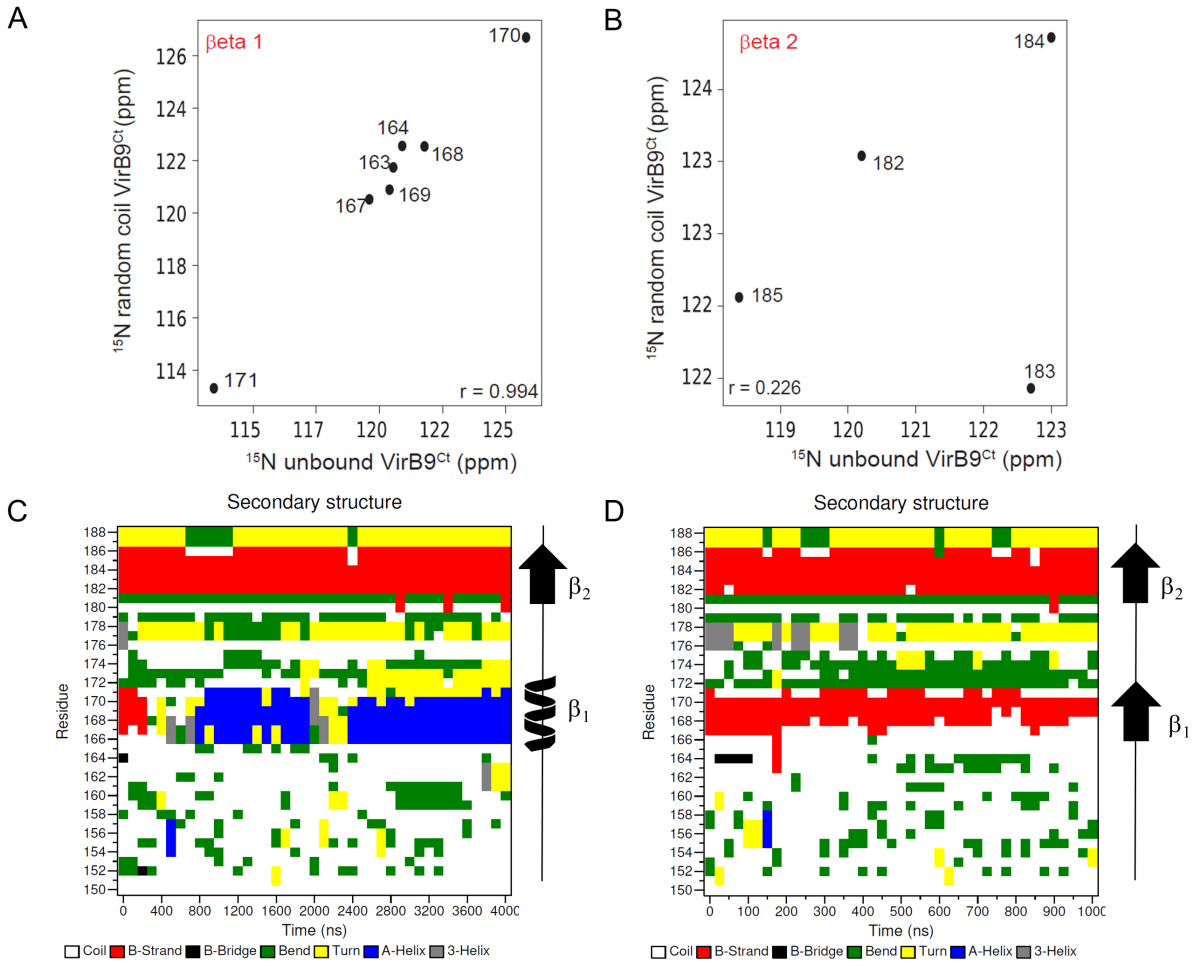

Figure 6: Comparison between the experimental backbone ^{15}N chemical shifts obtained for VirB9^{Ct} in the unbound state with the random coil ^{15}N chemical shifts predicted from the amino acid sequence.[60] Only residues located at the β_1 (A) and the β_2 (B) were analysed. Per-residue secondary structure of VirB9^{Ct} in the VirB7^{Nt}-unbound (C) and in the bound (D) states as a function of the simulation time. The dominant topology is shown on the right side.

Table 2: Experimental values of K_d^{app} obtained by ITC and calculated values of K_d^{int} at 25°C and 35°C.

Temperature	$K_d^{app}(\mu M)$	$K_d^{int}(\mu M)$
25°C	0.40	≈ 0.20
35°C	0.72	≈ 1.65

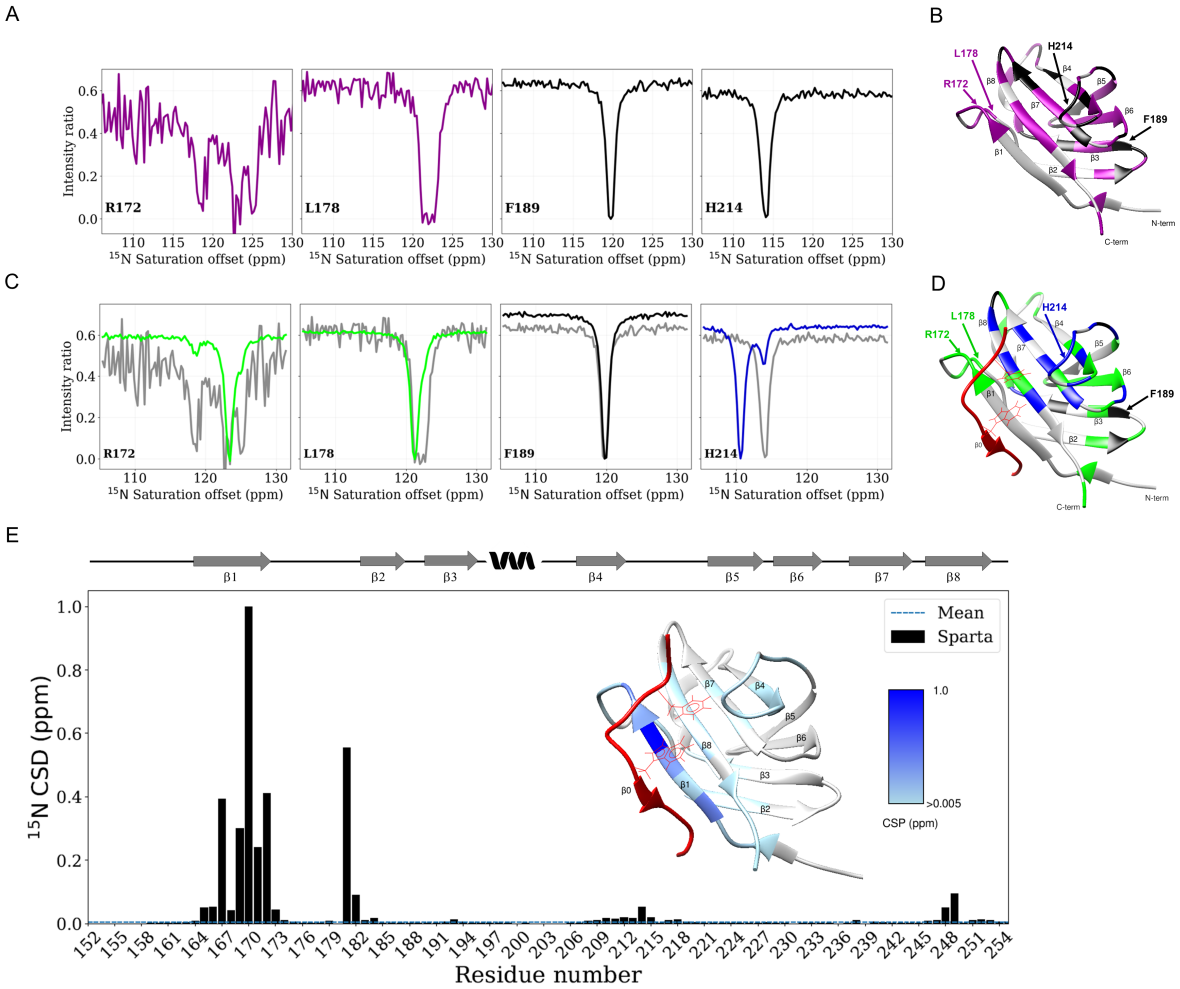

Figure 7: ^{15}N-CEST experiment recorded with VirB9^{Ct} in the absence of VirB7^{Nt}. Residues that showed multiple or broadened CEST dips suggestive of dynamics are color-coded magenta, while those that did not are color-coded black (A). VirB9^{Ct} residues displaying ^{15}N-CEST profiles according to R172 and L178, and F189 and H214 are color-coded magenta and black, respectively, on the structure of the complex (B). Comparison between the ^{15}N-CEST experiments recorded in the presence (colored) and absence (gray) of VirB7^{Nt} (C). Mapping of VirB9^{Ct} residues on the structure of the complex according to (C). VirB9^{Ct} Residues that showed significant ^{15}N chemical shift change upon binding to VirB7^{Nt} are shown in blue, while those that experienced no chemical shift change at all are colored black. Residues displaying the bound-like conformation in the absence of VirB7^{Nt} are color-coded green. VirB7^{Nt} is shown in red (D). ^{15}N chemical shift difference (CSD) between VirB9^{Ct} in the bound conformation in the presence and absence of VirB7^{Nt}. The ^{15}N chemical shifts for the bound state came from the BMRB entry 25512.[29] The chemical shifts for the unbound state were predicted with Sparta,[61] using the best model of the bound-state NMR structure (PDB 2N01) as input and the VirB7^{Nt} coordinates deleted. The inset shows the CSD values color-coded on the VirB9^{Ct}-VirB7^{Nt} NMR structure (PDB 2N01). The VirB9^{Ct} topology in complex is shown above and the VirB7^{Nt} peptide is shown in red (E).

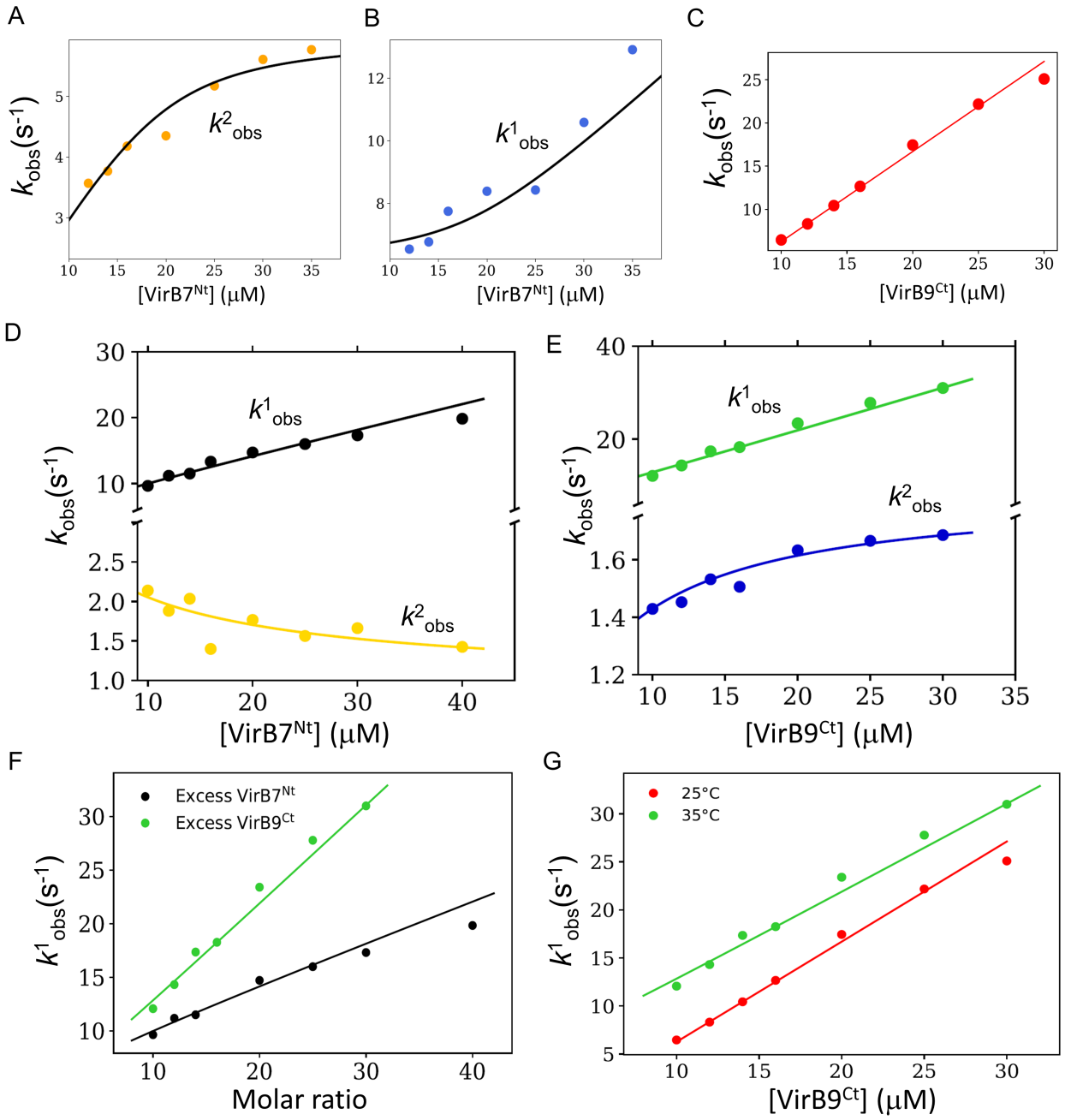

Figure 8: Observed kinetic rate constants from stopped flow fluorescence at 25°C under excess of VirB7^{Nt} (A and B) or under excess of VirB9^{Ct} (C), fitted to the CS and to the lock and key model, respectively. The observed kinetic rate constants obtained at 35°C under excess of VirB7^{Nt} fitted to the CS model (D) or under excess of VirB9^{Ct} fitted to the IF model (E). Comparison between the faster kinetic rate constants (k^1_{obs}) at 35 °C under excess of VirB7^{Nt} (black) or VirB9^{Ct}(green) (F). Faster kinetic rate constants obtained under excess of VirB9^{Ct} at 25 °C (red) and 35 °C (green) (G).

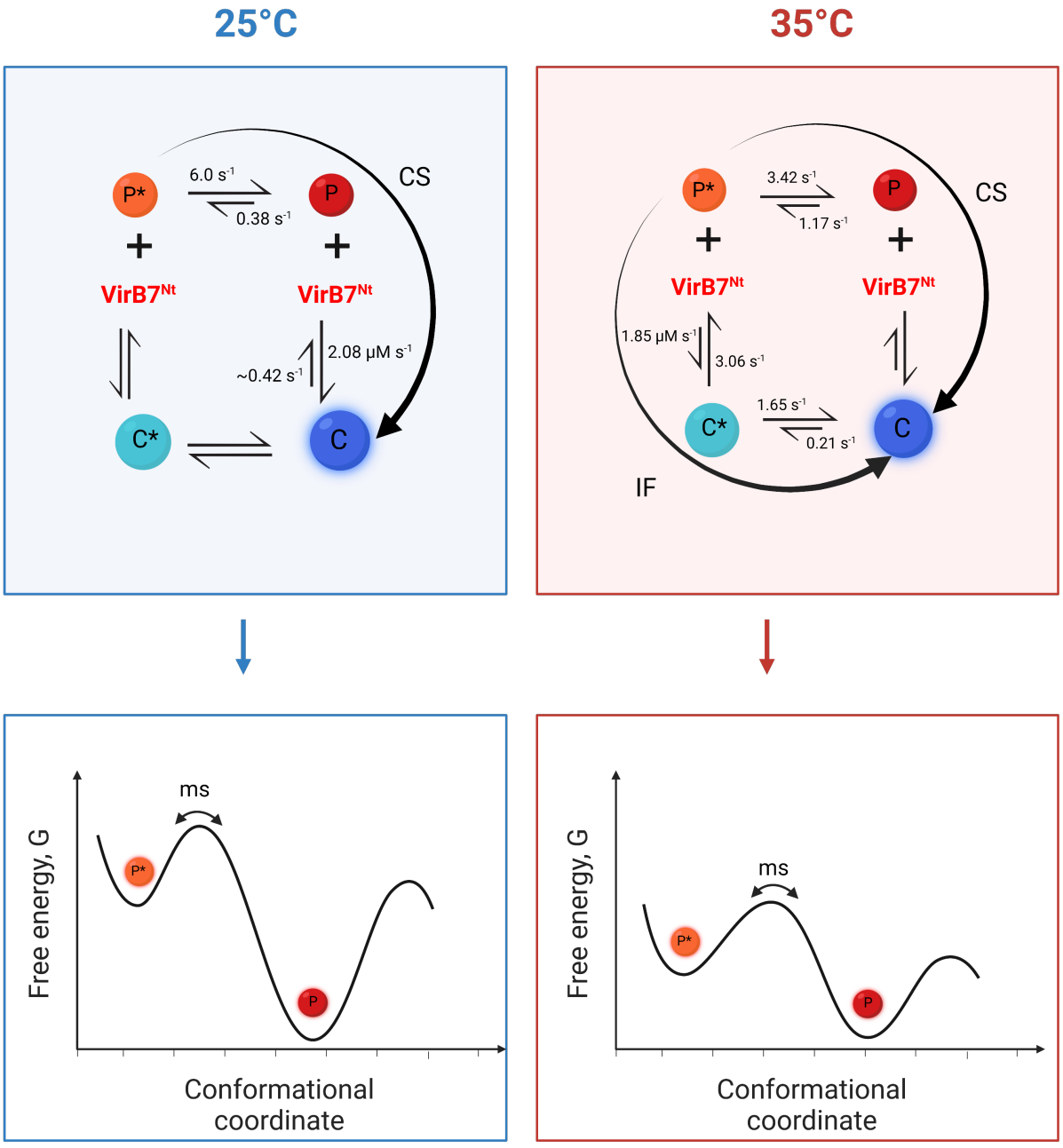

Figure 9: (Top) Possible VirB9^{Ct}-VirB7^{Nt} interaction pathways that were used to interpret the fluorescence stopped flow kinetic data obtained at 25 and 35 °C, with the kinetic rate constants of each step indicated on top of the corresponding arrow. (Bottom) Diagrams of the hypothetical conformational energy landscapes of the unbound VirB9^{Ct} at 25 and 35 °C highlighting the relative free energies of the P and the P* states. (Created with BioRender.com)

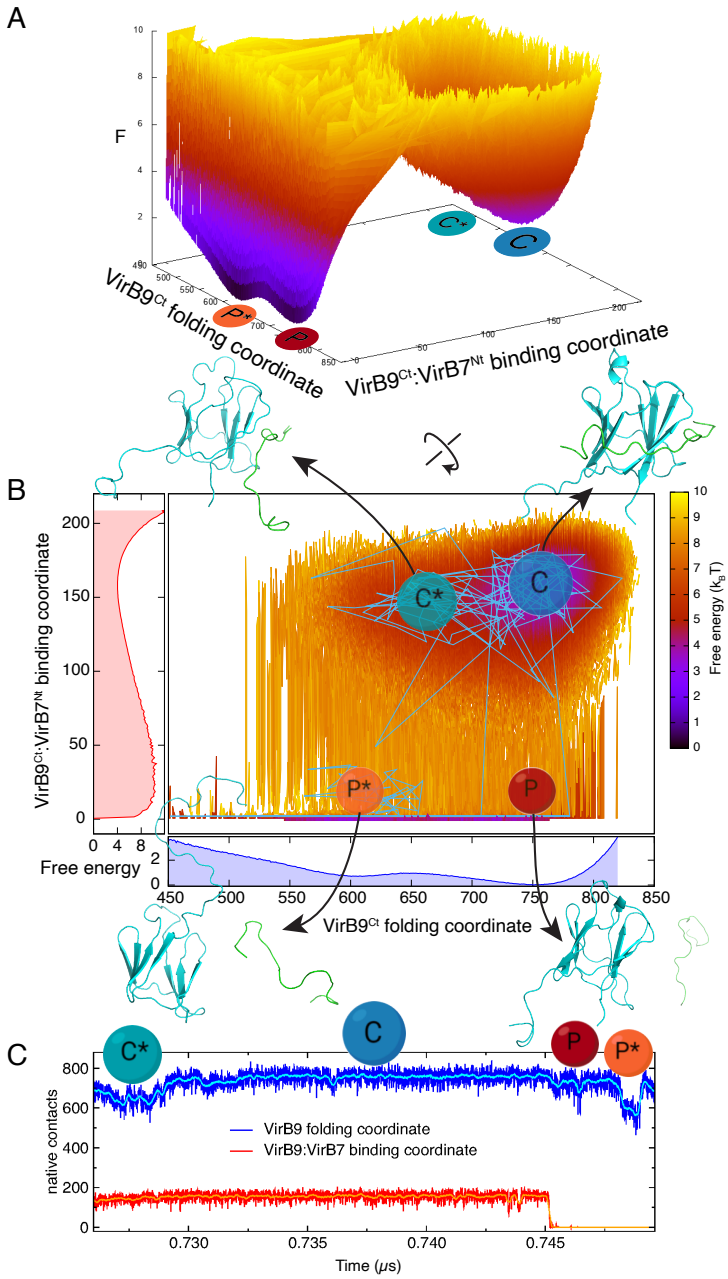

Figure 10: Simulation of the VirB9$^{\mathrm{Ct}}$-VirB7$^{\mathrm{Nt}}$ folding and binding free energy landscape using molecular dynamics. (A) Two-dimensional free energy (F) profile as a function of the number of VirB9$^{\mathrm{Ct}}$ intramolecular native contacts (Q_{fold}) and VirB7$^{\mathrm{Nt}}$-VirB9$^{\mathrm{Ct}}$ intermolecular contacts (Q_{bind}). (B) F in map view of (A) and the one-dimensional F projections as a function of Q_{bind} (in red) and of Q_{fold} (in blue). In (B), it is also shown an illustrative time trajectory of the protein complex projected over the F landscape with representative structures of the three F minima (P*, P and C) and of the metastable C* state. (C) Time trajectories of the reaction coordinates Q_{bind} (in red) and Q_{fold} (in blue) for the complex and their respective averages over each 50 frames in cyan and orange as guide to the eyes. (A) to (C) are presented at the binding temperature (T_{bind}) and F profiles are in units of the thermal k_BT with k_B being the Boltzmann constant.(Created with BioRender.com)

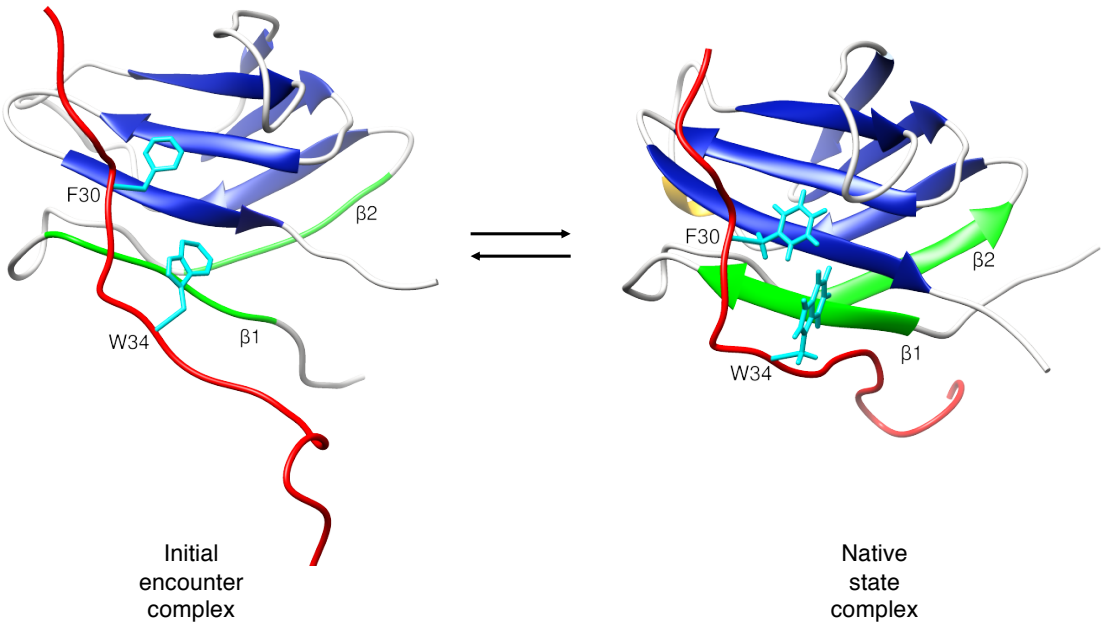

Figure 11: Snapshots of VirB7$^{\mathrm{Nt}}$-VirB9$^{\mathrm{Ct}}$ initial encounter (left) and native state (right) complexes, corresponding to the complex metastable state (C*) and the bound state (C) conformational energy basin of figure 10. VirB9$^{\mathrm{Ct}}$ β-strands β1 and β2 are colored green, while VirB7$^{\mathrm{Nt}}$ is shown in red. This orientation shows VirB7$^{\mathrm{Nt}}$ W34 and F30 positioned to make contacts with residues on the surface of the VirB9$^{\mathrm{Ct}}$ β1-β8-β7-β4 β-sheet.

Kinetic models

$$\mathrm{P}^* \underset{k_B}{\overset{k_A}{\rightleftharpoons}} \mathrm{P} \underset{k_{\mathrm{off}}}{\overset{k_{\mathrm{on}}[\mathrm{L}]}{\rightleftharpoons}} \mathrm{C}, \tag{1}$$

$$\mathrm{P} \underset{k_A}{\overset{k_B}{\rightleftharpoons}} \mathrm{P}^* \underset{k_{\mathrm{off}}}{\overset{k_{\mathrm{on}}[\mathrm{L}]}{\rightleftharpoons}} \mathrm{C}^* \underset{k_{\mathrm{D}}}{\overset{k_{\mathrm{C}}}{\rightleftharpoons}} \mathrm{C}. \tag{2}$$

Experimental

Expression and purification of VirB9$^{\mathrm{Ct}}$

BL21(DE3) *Escherichia coli* cells harboring the plasmid pET28a containing the gene encoding VirB9$^{\mathrm{Ct}}$ (residues 154-255) were grown in either M9 or LB medium supplemented with 50 μg/ml of kanamycin at 37 °C.[29] Isotopically enriched protein samples were expressed in M9 in the presence of 2 g/l and/or 0.5 g/l of ^{13}C uniformly labeled glucose and ^{15}N ammonium chloride, respectively. Protein expression was induced by the addition of 0.5 mM of isopropyl-1-thio-β-D-galactopyranoside (IPTG) when the optical density at 600 nm (O.D$_{600}$) reached 0.8 and carried out overnight at 18 °C. Cells were harvested by centrifugation for 1 hour at 5000 rpm and 4 °C on a Beckman centrifuge using rotor JLA-10. The cell pellet was suspended in lysis buffer (20 mM Tris/HCL pH 7.5, 1 mM PMSF, 0.5 mg/mL lysozyme) and stored at -20 °C until further use. Cell lysis was carried out by sonication. The lysate was clarified by centrifugation for 1 hour at 13000 rpm on a Beckman centrifuge equipped with rotor JA-20. The supernatant was loaded on a Hiprep FF 16/10 SP Sepharose column (GE Healthcare), pre-equilibrated with buffer A (20 mM Tris/HCL pH 7.5). VirB9$^{\mathrm{Ct}}$ eluted during a linear NaCl gradient with buffer B (20 mM Tris/HCl pH 7.5 and 700 mM NaCl) over 14 column volumes (CV). Eluted fractions were pooled and loaded onto a Ni^{2+}-HiTrap column (GE Healthcare), pre-equilibrated with buffer A (20 mM Tris/HCl pH 7.5, 200 mM NaCl and 20 mM imidazole). VirB9$^{\mathrm{Ct}}$ eluted during a linear concentration gradient of imidazole with buffer B (20 mM Tris/HCl pH 7.5, 200 mM NaCl and 500 mM imidazole). The

imidazole was removed by buffer exchange to 20 mM Tris/HCl pH 7.5, and VirB9^{Ct} was concentrated to a final volume of 1 ml using an Amicon Ultra Device with cutoff of 3 kDa. Cleavage of the histidines tag was carried out by a 3 hours incubation with 100-200 μl of thrombin-agarose resin (Sigma-Aldrich) in 50 mM Tris-HCl pH 8.0 containing 10 mM $CaCl_2$. Subsequently, this sample was loaded onto the Ni^{2+}-HiTrap column equilibrated with buffer A and cut VirB9^{Ct} was found in the flowthrough. The isolated protein buffer was exchanged to 20 mM sodium acetate pH 5.5 containing 50 mM NaCl. Concentrated protein samples were stored at 4 °C or frozen at 20 °C until further use. Protein concentration was calculated from the absorbance at 280 nm using the molar extinction coefficient $\epsilon = 17420 M^{-1}cm^{-1}$.

Preparation of the VirB7^{Nt} peptide

A synthetic peptide with the amino acid sequence TKPAPDFGGR WKHVNHFDEAPTE, corresponding to VirB7 residues 24 to 46 (VirB7^{Nt}), was purchased from Biomatik. The peptide was acetylated at the N-terminal end and amidated at the C-terminal end. VirB7^{Nt} samples were prepared by dissolving the required peptide mass in 20 mM sodium acetate pH 5.5 with 50 mM NaCl, or in 20 mM sodium phosphate pH 7.5 with 10 mM NaCl. Peptide concentration was calculated by the absorbance at 280 nm assuming $\epsilon = 5500\ M^{-1}cm^{-1}$.

NMR experiments

All NMR measurements were performed on a Bruker AVANCE III spectrometer operating at 800 MHz (^{1}H field) and equipped with a TCI cryoprobe. All NMR spectra were processed with NMRPipe and analyzed using the CcpNmr Analysis software version 2.4.[62,63] NMR samples contained approximately 500μM of protein dissolved in 20 mM sodium acetate pH 5.5, containing 50 mM of NaCl and 10% of D_2O. Sub-stoichiometric VirB9^{Ct}-VirB7^{Nt} samples used for the CEST experiments were prepared by adding the appropriate amount of unlabeled VirB7^{Nt} dissolved in the same buffer as VirB9^{Ct}. CEST experiments were recorded in pseudo-3D fashion by incrementing the weak ^{15}N saturation field carrier frequency dur-

ing the exchange period, T_{ex}, of 400 ms. A reference spectrum was recorded skipping the exchange period. CEST I/I_0 profiles were extracted and visualized using *in-house* scripts made for MATLAB R2015a or Python. The ^{15}N-CEST I/I_0 profiles recorded with weak saturation frequencies $\gamma_N B_1/2\pi = 15$ and 30 Hz were simultaneously fitted to the Bloch-McConnell equation assuming a two-states exchange model using an in-house Python script that uses a Bayesian approach as described.[64] Uncertainties in the cross peak intensities were taken from the noise level in each spectrum. The $\gamma_N B_1/2\pi$ saturation field and the experimental bound state ^{15}N chemical shifts (Ω_B) were constrained with Gaussian priors of $\sigma = 1\%$ and 5%, respectively. VirB9^{Ct} random coil ^{15}N chemical shifts were predicted using the online predictor server ncIDP.[60] Backbone (^{1}HN, ^{15}N, $^{13}C\alpha$, ^{13}CO) and side chain ($^{13}C\beta$) resonance assignments for VirB9^{Ct} in the unbound state were obtained through the analysis of a set of triple resonance NMR experiments recorded at 7 °C and deposited in the BMRB under the accession code 51836. Assignments for the unbound VirB9^{Ct} ^{1}H-^{15}N cross peaks at 35 °C **(Figure S5)** were transferred from those obtained at 7 °C using a series of HSQC experiments recorded at increasing temperatures from 7 up to 35 °C in steps of 3 °C. Additional assignments were obtained from the analysis of a longitudinal exchange HSQC experiment,[65] recorded with a mixing time of 400 ms on a sample of ^{15}N labeled VirB9^{Ct} and unlabeled VirB7^{Nt} at the 1:06 (VirB9^{Ct}:VirB7^{Nt}) molar ratio. Using this approach 83 ^{1}H-^{15}N spin pairs were assigned at 35 °C and deposited in the BMRB under the accession code 52005. Backbone resonance assignments for VirB9^{Ct} and VirB7^{Nt} in the bound state (35 °C) were obtained from the BMRB entry 25512.[29]

Circular Dichroism

Circular Dichroism (CD) spectra were recorded on a Jasco J720 (Jasco, Japan) spectropolarimeter at 25°C, from 190 to 260 nm using integration step of 1 nm, scanning speed of 50 nm/min and accumulation of 6 scans. Samples were prepared at 10 μM protein concentration in 20 mM sodium phosphate pH 7.26 with 10 mM NaCl, and transferred to 1 mm

path-length quartz cells. A spectrum of the buffer was recorded with the same acquisition parameters as the protein sample and subtracted as blank. Deconvolution of the VirB9$^{\mathrm{Ct}}$ CD spectrum was carried out with the online server DICHROWEB using the CDSSTR method and dataset # 7 that includes globular and denatured protein spectra[35,66,67] . Denaturation experiments were performed on a Jasco J-815 spectropolarimeter using a 1 mm path-length cell. Far UV-CD spectra were recorded from 190 to 260 nm, using integration step of 1 nm, scanning speed of 100 nm/min and accumulation of 3 scans. The temperature was increased from 25 °C to 95 °C in steps of 5°C. The behavior of the elipticity at at 215 nm and 233 nm as a function of temperature was fitted to the following equation assuming a two state equilibrium:

$$\Theta_\lambda(T) = S_N \left(\frac{1}{1 + \exp \frac{-\Delta H}{RT}\left(1 - \frac{T}{T_m}\right)} \right) + S_D \left(\frac{1}{1 + \exp \frac{\Delta H}{RT}\left(1 - \frac{T}{T_m}\right)} \right), \tag{3}$$

where θ, S_N and S_D refer to the observed, native state and denatured state elipticities, respectively, at a given wavelength. The terms within brackets refer to the populations of native and denatured states. ΔH and T$_m$ refer to the denaturation enthalphy and the melting temperature, respectively. Fitting to Eq. 3 assumed ΔH, T_{m}, S_N and S_D as free parameters. The sloping baselines before and after the denaturation transition were modeled replacing the S$_{\mathrm{N}}$ and/or S$_{\mathrm{D}}$ signal with a straight line equation as function of temperature:

$$S_{\mathrm{N/D}}(T) = mT + b, \tag{4}$$

where T is the temperature, m is the slope and b is the intercept with the y axis.[68–70]

ANS Fluorescence

The fluorescence spectra of 1-anilino-8-naphthalenesulfonic acid (ANS) were recorded with a Hitachi F-7000 FL spectrofluorometer using excitation wavelength (λ_{ex}) of 375 nm. The

emission wavelength (λ_{em}) was scanned from 400 nm to 650 nm at 25 °C. A 2 mM ANS stock solution was prepared in 20 mM sodium acetate buffer (pH 5.5) containing 50 mM NaCl. Stock protein and peptide solutions were prepared in the same buffer. The ANS concentration was estimated using $\epsilon_{350} = 4950 M^{-1} cm^{-1}$.[71] All fluorescence samples consisted of 10 μM of protein and/or peptide plus 250 μM of ANS in the same buffer. Samples were pre-incubated for 30 minutes before fluorescence measurements.

Isothermal Titration Calorimetry

Isothermal titration calorimetry experiments were performed on a VP-ITC micro calorimeter (MicroCal incorporated). Protein and peptide samples were prepared in the same buffer that consisted in 20 mM sodium acetate pH 5.5 and 50 mM NaCl. All measurements were performed in triplicate, at temperatures of 10, 25 and 35 °C. Titrations were carried out with 20 μM of VirB7^{Nt} peptide in the calorimeter cell and 200 μM of VirB9^{Ct} in the syringe using 20-25 injections of 5 μl. Control experiments were carried out by titrating buffer in the peptide. Data analysis was carried out using OriginLab7.0 and the standard supplier software for K_d and ΔH estimation. Additionally, a set titrations of the peptide at 10, 15 and 20 μM with VirB9^{Ct} at 150 μM were carried out at 35 °C. The resulting isotherms crossed each other at the same inflexion point; they were simultaneously fitted to the one-site binding stoichiometric model to determine the K_d^{app} at 35 °C as described previously.[64] Briefly, the stoichiometry of the complex was constrained at $n = 1$ with a narrow Gaussian prior with $\sigma = 0.01$, while the peptide concentrations were allowed to vary as free parameters.

Differential Scanning Calorimetry

Differential scanning calorimetry experiments were performed on a VP-DSC micro-calorimeter (MicroCal incorporated) with a scan rate of 60°C/h. All samples were prepared in 20 mM sodium acetate pH 5.5 containing 50 mM of NaCl. The concentrations of the unbound VirB9^{Ct} and of the VirB9^{Ct}-VirB7^{Nt} 1:1 complex were 300 μM. All measurements were

performed in triplicate and were reproducible.

Stopped flow kinetics

Kinetic experiments were carried out using an Applied Photophysics stopped-flow spectrofluorometer. The reaction course was followed by measuring the VirB7$^{\mathrm{Nt}}$ and VirB9$^{\mathrm{Ct}}$ Trp fluorescence intensities at $\lambda_{\mathrm{em}} = 350$nm, with $\lambda_{\mathrm{ex}} = 280$nm. Samples were prepared in 20 mM sodium acetate pH 5.5, containing 50 mM of NaCl. All experiments were performed under pseudo-first order conditions at 1 μM concentrations of VirB9$^{\mathrm{Ct}}$ or VirB7$^{\mathrm{Nt}}$ with increasing VirB9$^{\mathrm{Ct}}$ or VirB7$^{\mathrm{Nt}}$ concentrations (from 10 up to 40 μM), respectively. Each kinetic trace was fitted to either single or double exponential functions using the proData software (Applied photophysics) to extract the observed rate constant(s) (k_{obs}) at each concentration. Each k_{obs} corresponded to the average k_{obs} value from 3-5 fitted traces.

The kinetic data at 25 °C recorded under excess of [VirB7$^{\mathrm{Nt}}$] was fitted to Eq. 5, corresponding to the general CS case (Scheme. 1):[51,53]

$$k_{\mathrm{obs}}^{1,2}(x) = \frac{1}{2}\left[(k_{\mathrm{on}}x + k_{\mathrm{off}} + k_{\mathrm{A}} + k_{\mathrm{B}}) \pm \sqrt{(k_{\mathrm{on}}x + k_{\mathrm{off}} - k_{\mathrm{A}} - k_{\mathrm{B}})^2 + 4k_{\mathrm{B}}k_{\mathrm{on}}x}\right], \qquad (5)$$

where x denotes the VirB7$^{\mathrm{Nt}}$ (under pseudo first order condition for VirB7$^{\mathrm{Nt}}$) or VirB9$^{\mathrm{Ct}}$ (under reverse pseudo first order condition) concentrations.

The experimental data at 35°C were fitted to the combined CS-IF model (Scheme 2). Briefly, k_{obs}^2 values obtained under excess of VirB7$^{\mathrm{Nt}}$ were adjusted with the CS part of the model assuming the rapid equilibrium approximation according to Eq. 6:

$$k_{\mathrm{obs}} = k_{\mathrm{A}} + k_{\mathrm{B}}\frac{K_{\mathrm{d}}^{\mathrm{int}}}{K_{\mathrm{d}}^{\mathrm{int}} + [L]}, \qquad (6)$$

where $K_{\mathrm{d}}^{\mathrm{int}}$ refers to the intrinsic K_{d} given by $k_{\mathrm{off}}/k_{\mathrm{on}}$. The values of k_{obs}^1 and k_{obs}^2 obtained

under excess of VirB9^{Ct} were adjusted with Eq. 7, corresponding to the IF part of the model:

$$k_{obs}^{1,2}(x) = \frac{1}{2}\left[(k_{on}x + k_{off} + k_C + k_D) \pm \sqrt{(k_{on}x + k_{off} - k_D - k_C)^2 + 4k_{off}k_C}\right]. \quad (7)$$

To further restrict the parameters' space we used the K_d^{app} obtained by ITC at 35 °C as an additional experimental information. It is worthy noting that K_d^{app} and K_d^{int} depend on each other according to the following relation:

$$K_d^{app} \equiv \frac{\left(1 + \frac{k_B}{k_A}\right) K_d^{int}}{\left(1 + \frac{k_C}{k_D}\right)}. \quad (8)$$

In the CS-IF combined model the independent CS and IF steps share the same binding event. Overall the fitting was implemented in a Python routine using a Bayesian approach, considering k_{on}, k_{off}, k_A, k_B, k_C and k_D as free parameters, while k_{obs2} obtained under excess of VirB7^{Nt} and k_{obs1} and k_{obs2} obtained under excess of VirB9^{Ct}, as well as the K_d^{app} obtained from ITC at 35°C, were given as input. The latter was constrained by a Gaussian prior with a value centered at $K_d^{app} = 0.723\mu$M and a confidence interval of 0.082 μM. MCMC sampling was carried out with 200 chains of 3000 points each, and a burning of 2000 points. Flat priors were introduced to restraint the range of the free parameters: $0.001 \leq k_A \leq 10.0$, $0.001 \leq k_B \leq 10.0$, $0.001 \leq k_{on} \leq 10.0$, $0.001 \leq k_{off} \leq 10.0$, $0.001 \leq k_C \leq 10.0$ and $0.00001 \leq k_D \leq 2.0$ in units of s^{-1}. Fitted parameters probability distributions and their correlations are shown in the **Supplementary Figure S8**.

Molecular dynamic simulations

MD simulations of unbound and bound VirB9^{Ct}

Molecular dynamic (MD) simulations of unbound and bound VirB9^{Ct} were computed using Amber FF99SBnmr2 forcefield.[72] The first model of the VirB9^{Ct}-VirB7^{Nt} NMR ensemble (PDB 2N01) was used as starting structure. For the unbound VirB9^{Ct} computer simula-

tion, we removed the peptide from the model using the UCFS chimera tool. The system conditions were prepared using GROMACS v2018.6.[73] All systems were then explicitly solvated with TIP4P water models in a cubic box (10.5 X 7.0 X 7.0 nm) and neutralized keeping NaCl concentration at 50 mM (15 Na+ and 23 Cl- ions). Protein charges at pH 5.0 were determined using Propka version 3.0.[74] The systems were equilibrated consecutively in isothermal-isochoric (NVT) and isothermal-isobaric (1 bar; NpT) ensembles at 308 K for 2000 ps. The unbound and bound VirB9^{Ct} MD simulations were run for 4000 and 1000 ns, respectively.

MD simulation of the interaction mechanism

The structure-based model (SBM),[75] formerly known as Go-model[76] has its foundation on the energy landscape theory.[57] SBM was used to simulate the VirB9^{Ct}-VirB7^{Nt} complex with all-heavy (non-hydrogen) atoms. SBMs is a topology-based model that defines the energy minimum of the Hamiltonian function as the native conformation[77,78] i.e, the model has minimal intrinsic energetic frustration.[79,80] The simulation protocol was based in the previous works.[59,81] SMOG2 version 2.3-beta with standard options for the all-atom model prepared the input files for the SBM simulations.[82] Simulations were executed with the GROMACS suite 5.1.4.[73] The thermodynamic analysis was performed over 50 temperature runs from lower temperatures (fully folded and bound states) to higher temperatures (unbound states), including the transition temperature between the on and off states (T_{bind}). Each simulation was executed over 1 μs with integration steps of 2 fs and snapshots were recorded every 4 ps. The results are shown in reduced units of GROMACS for temperature and energy, commonly used in coarse-grained SBMs.[75] Thus, energy is in units of k_BT, and the time unit is not as the real one. Thermodynamic calculations were executed by the Weighted Histogram Analysis Method (WHAM)[56,83] implemented in the PyWham package and BASH scripts.[84] WHAM computes the microcanonical density of states that is used to build the free energy profiles. T_{bind} was defined as the peak found in the theoretical specific heat curve

in temperature (C_v(T)). The number/fraction of native contacts within a given structure (Q) was used to evaluate the nativeness along the reaction coordinate, which describes how similar is a given structure with respect to the reference native structure. Root mean square fluctuation (rmsf), radius of gyration (R_g), root mean square deviation (rmsd) and distance between two chains (d) were computed with the analysis package contained in the GROMACS suite. Protein structures were visualized with PyMOL (`https://pymol.org`), VMD[85] and UCSF Chimera[86] softwares. Two and three dimensional curves were plotted with Grace (`https://plasma-gate.weizmann.ac.il/Grace`), Gnuplot (`http://www.gnuplot.info`) and Matplotlib[87] packages. The analysis codes were implemented in Python (`https://python.org`) using Jupyter Notebooks with native libraries, such as NumPy, SciPy and Pandas.

Acknowledgement

The authors thank the Analytical Instrumentation Center of the University of São Paulo for providing access to the 800 MHz NMR instrument. This work was supported by grants from the São Paulo Research Foundation (FAPESP 2017/17303-7), the Minas Gerais Research Foundation (FAPEMIG APQ-02303-21) and the Conselho Nacional de Desenvolvimento Científico e Tecnológico (CNPq 312328/2019-2). Computational resources were provided by the "Núcleo de Computação Científica da Universidade do Estado de São Paulo" (NCC/GridUnesp) and the "Centro Nacional de Processamento de Alto Desempenho" in São Paulo (CENAPAD-SP). ALD received a CNPq PhD fellowship (141398/2018-3). RKS receives a CNPq research fellowship (308119/2020-7). JDR and MVCC received FAPESP post-doctoral fellowships (2018/21450-8 and 2016/17375-5).

Supporting Information Available

Supplemental data is available.

References

(1) Dunker, A. et al. Intrinsically disordered protein. *Journal of Molecular Graphics and Modelling* **2001**, *19*, 26–59.

(2) Uversky, V. N.; Dunker, A. K. Understanding protein non-folding. *Biochimica et Biophysica Acta - Proteins and Proteomics* **2010**, *1804*, 1231–1264.

(3) Tompa, P. Intrinsically unstructured proteins. *Trends in Biochemical Sciences* **2002**, *27*, 527–533.

(4) Dyson, H. J.; Wright, P. E. Intrinsically unstructured proteins and their functions. *Nature Reviews Molecular Cell Biology* **2005**, *6*, 197–208.

(5) Van Der Lee, R. et al. Classification of intrinsically disordered regions and proteins. *Chemical Reviews* **2014**, *114*, 6589–6631.

(6) Fuxreiter, M. Fuzziness in Protein Interactions—A Historical Perspective. *Journal of Molecular Biology* **2018**, *430*, 2278–2287.

(7) Mollica, L.; Bessa, L. M.; Hanoulle, X.; Jensen, M. R.; Blackledge, M.; Schneider, R. Binding mechanisms of intrinsically disordered proteins: Theory, simulation, and experiment. *Frontiers in Molecular Biosciences* **2016**, *3*.

(8) Tompa, P.; Fuxreiter, M. Fuzzy complexes: polymorphism and structural disorder in protein–protein interactions. *Trends in biochemical sciences* **2008**, *33*, 2–8.

(9) Morris, O. M.; Torpey, J. H.; Isaacson, R. L. Intrinsically disordered proteins: modes of binding with emphasis on disordered domains. *Open Biology* **2021**, *11*, 210222.

(10) Yang, J.; Gao, M.; Xiong, J.; Su, Z.; Huang, Y. Features of molecular recognition of intrinsically disordered proteins via coupled folding and binding. *Protein Science* **2019**, *28*, 1952–1965.

(11) BHATTARAI, A.; EMERSON, I. A. Dynamic conformational flexibility and molecular interactions of intrinsically disordered proteins. *J Biosci* **2020**, *0123456789*, 1–17.

(12) Bugge, K.; Brakti, I.; Fernandes, C. B.; Dreier, J. E.; Lundsgaard, J. E.; Olsen, J. G.; Skriver, K.; Kragelund, B. B. Interactions by Disorder – A Matter of Context. *Frontiers in Molecular Biosciences* **2020**, *7*.

(13) Toto, A.; Malagrino, F.; Visconti, L.; Troilo, F.; Pagano, L.; Brunori, M.; Jemth, P.; Gianni, S. Templated folding of intrinsically disordered proteins. *Journal of Biological Chemistry* **2020**, *295*, 6586–6593.

(14) Dyson, H. J.; Wright, P. E. Coupling of folding and binding for unstructured proteins. *Current opinion in structural biology* **2002**, *12*, 54–60.

(15) Toto, A.; Troilo, F.; Visconti, L.; Malagrino, F.; Bignon, C.; Longhi, S.; Gianni, S. Binding induced folding: Lessons from the kinetics of interaction between NTAIL and XD. *Archives of Biochemistry and Biophysics* **2019**, *671*, 255–261.

(16) Monod, J.; Wyman, J.; Changeux, J.-P. On the nature of allosteric transitions: A plausible model. *Journal of Molecular Biology* **1965**, *12*, 88–118.

(17) Koshland, D. E. Application of a Theory of Enzyme Specificity to Protein Synthesis. *Proceedings of the National Academy of Sciences* **1958**, *44*, 98–104.

(18) Ma, B.; Kumar, S.; Tsai, C.-J.; Nussinov, R. Folding funnels and binding mechanisms. *Protein engineering* **1999**, *12*, 713–720.

(19) Levy, Y.; Cho, S. S.; Onuchic, J. N.; Wolynes, P. G. A survey of flexible protein binding mechanisms and their transition states using native topology based energy landscapes. *Journal of molecular biology* **2005**, *346*, 1121–1145.

(20) Tsai, C.-J.; Kumar, S.; Ma, B.; Nussinov, R. Folding funnels, binding funnels, and protein function. *Protein Science* **1999**, *8*, 1181–1190.

(21) Hammes, G. G.; Chang, Y. C.; Oas, T. G. Conformational selection or induced fit: A flux description of reaction mechanism. *Proceedings of the National Academy of Sciences of the United States of America* **2009**, *106*, 13737–13741.

(22) Shammas, S. L.; Crabtree, M. D.; Dahal, L.; Wicky, B. I.; Clarke, J. Insights into coupled folding and binding mechanisms from kinetic studies. *Journal of Biological Chemistry* **2016**, *291*, 6689–6695.

(23) Sugase, K.; Dyson, H. J.; Wright, P. E. Mechanism of coupled folding and binding of an intrinsically disordered protein. *Nature* **2007**, *447*, 1021–1025.

(24) Schneider, R.; Maurin, D.; Communie, G.; Kragelj, J.; Hansen, D. F.; Ruigrok, R. W.; Jensen, M. R.; Blackledge, M. Visualizing the molecular recognition trajectory of an intrinsically disordered protein using multinuclear relaxation dispersion NMR. *Journal of the American Chemical Society* **2015**, *137*, 1220–1229.

(25) Malagrinò, F.; Diop, A.; Pagano, L.; Nardella, C.; Toto, A.; Gianni, S. Unveiling induced folding of intrinsically disordered proteins–Protein engineering, frustration and emerging themes. *Current Opinion in Structural Biology* **2022**, *72*, 153–160.

(26) Meir, A.; Macé, K.; Vegunta, Y.; Williams, S. M.; Waksman, G. Substrate recruitment mechanism by gram-negative type III, IV, and VI bacterial injectisomes. *Trends in Microbiology* **2023**,

(27) Souza, D. P.; Oka, G. U.; Alvarez-Martinez, C. E.; Bisson-Filho, A. W.; Dunger, G.; Hobeika, L.; Cavalcante, N. S.; Alegria, M. C.; Barbosa, L. R.; Salinas, R. K.; Guzzo, C. R.; Farah, C. S. Bacterial killing via a type IV secretion system. *Nature Communications* **2015**, *6*, 1–9.

(28) Sgro, G. G.; Costa, T. R.; Cenens, W.; Souza, D. P.; Cassago, A.; Coutinho de Oliveira, L.; Salinas, R. K.; Portugal, R. V.; Farah, C. S.; Waksman, G. Cryo-EM struc-

ture of the bacteria-killing type IV secretion system core complex from Xanthomonas citri. *Nature Microbiology* **2018**, *3*, 1429–1440.

(29) Oliveira, L. C.; Souza, D. P.; Oka, G. U.; Lima, F. d. S.; Oliveira, R. J.; Favaro, D. C.; Wienk, H.; Boelens, R.; Farah, C. S.; Salinas, R. K. VirB7 and VirB9 Interactions Are Required for the Assembly and Antibacterial Activity of a Type IV Secretion System. *Structure* **2016**, *24*, 1707–1718.

(30) Souza, D. P.; Andrade, M. O.; Alvarez-Martinez, C. E.; Arantes, G. M.; Farah, C. S.; Salinas, R. K. A component of the Xanthomonadaceae type IV secretion system combines a VirB7 motif with a N0 domain found in outer membrane transport proteins. *PLoS Pathogens* **2011**, *7*.

(31) Saxena, V. P.; Wetlaufer, D. B. A new basis for interpreting the circular dichroic spectra of proteins. *Proceedings of the National Academy of Sciences of the United States of America* **1971**, *68*, 969–972.

(32) Woody, R. W. Aromatic side-chain contributions to the far ultraviolet circular dichroism of peptides and proteins. *Biopolymers* **1978**, *17*, 1451–1467.

(33) Grishina, I. B.; Woody, R. W. Contributions of tryptophan side chains to the circular dichroism of globular proteins: Exciton couplets and coupled oscillators. *Faraday Discussions* **1994**, *99*, 245–262.

(34) Woody, R. W. Contributions of tryptophan side chains to the far-ultraviolet circular dichroism of proteins. *European Biophysics Journal* **1994**, *23*, 253–262.

(35) Miles, A. J.; Ramalli, S. G.; Wallace, B. A. DichroWeb, a website for calculating protein secondary structure from circular dichroism spectroscopic data. *Protein Science* **2022**, *31*, 37–46.

(36) Semisotnov, G. V.; Rodionova, N. A.; Razgulyaev, O. I.; Uversky, V. N.; Gripas', A. F.; Gilmanshin, R. I. Study of the "molten globule" intermediate state in protein folding by a hydrophobic fluorescent probe. *Biopolymers* **1991**, *31*, 119–128.

(37) Stryer, L. The interaction of a naphthalene dye with apomyoglobin and apohemoglobin: A fluorescent probe of non-polar binding sites. *Journal of Molecular Biology* **1965**, *13*, 482–495.

(38) Barone, G.; Catanzano, F.; Del Vecchio, P.; Giancola, C.; Graziano, G. Differential scanning calorimetry as a tool to study protein-ligand interactions. *Pure and Applied Chemistry* **1995**, *67*, 1867–1872.

(39) Hendrix, T.; Griko, Y. V.; Privalov, P. L. A calorimetric study of the influence of calcium on the stability of bovine α-lactalbumin. *Biophysical Chemistry* **2000**, *84*, 27–34.

(40) González, M.; Argaraña, C. E.; Fidelio, G. D. Extremely high thermal stability of streptavidin and avidin upon biotin binding. *Biomolecular Engineering* **1999**, *16*, 67–72.

(41) Johnson, C. M. Differential scanning calorimetry as a tool for protein folding and stability. *Archives of Biochemistry and Biophysics* **2013**, *531*, 100–109.

(42) Celej, M. S.; Fidelio, G. D.; Dassie, S. A. Protein unfolding coupled to ligand binding: Differential scanning calorimetry simulation approach. *Journal of Chemical Education* **2005**, *82*, 85–92.

(43) Pucci, F.; Rooman, M. Physical and molecular bases of protein thermal stability and cold adaptation. *Current Opinion in Structural Biology* **2017**, *42*, 117–128.

(44) Layton, C. J.; Hellinga, H. W. Thermodynamic analysis of ligand-induced changes in protein thermal unfolding applied to high-throughput determination of ligand affinities with extrinsic fluorescent dyes. *Biochemistry* **2010**, *49*, 10831–10841.

(45) Perozzo, R.; Folkers, G.; Scapozza, L. Thermodynamics of Protein – Ligand Interactions : History , Presence , and Future Aspects. *Journal of receptors and signal transductions* **2004**, *24*, 1–51.

(46) Du, X.; Li, Y.; Xia, Y. L.; Ai, S. M.; Liang, J.; Sang, P.; Ji, X. L.; Liu, S. Q. Insights into protein–ligand interactions: Mechanisms, models, and methods. *International Journal of Molecular Sciences* **2016**, *17*, 1–34.

(47) Spolar, R. S.; Record, M. T. Coupling of Local Folding to Site-Specific Binding of Proteins to DNA. *Science* **1994**, *263*, 777–784.

(48) Vega, S.; Abian, O.; Velazquez-Campoy, A. On the link between conformational changes, ligand binding and heat capacity. *Biochimica et Biophysica Acta - General Subjects* **2016**, *1860*, 868–878.

(49) Schön, A.; Freire, E. *Methods in Molecular Biology*; Methods in Molecular Biology; Humana Press Inc., 2020; pp 449–462, Publisher Copyright: © Springer Science+Business Media, LLC, part of Springer Nature 2020.

(50) Shen, Y.; Delaglio, F.; Cornilescu, G.; Bax, A. TALOS+: A hybrid method for predicting protein backbone torsion angles from NMR chemical shifts. *Journal of Biomolecular NMR* **2009**, *44*, 213–223.

(51) Di Cera, E. Mechanisms of ligand binding. *Biophysics Reviews* **2020**, *1*, 011303.

(52) Cliver R. Bagshaw, *Biomolecular kinetics : a step-by-step guide*; 2017; p 470.

(53) Vogt, A. D.; Di Cera, E. Conformational selection or induced fit? A critical appraisal of the kinetic mechanism. *Biochemistry* **2012**, *51*, 5894–5902.

(54) Gianni, S.; Dogan, J.; Jemth, P. Distinguishing induced fit from conformational selection. *Biophysical Chemistry* **2014**, *189*, 33–39.

(55) Floor, M.; Li, K.; Estévez-Gay, M.; Agulló, L.; Muñoz-Torres, P. M.; Hwang, J. K.; Osuna, S.; Villà-Freixa, J. SBMOpenMM: A Builder of Structure-Based Models for OpenMM. *Journal of Chemical Information and Modeling* **2021**, *61*, 3166–3171, PMID: 34251801.

(56) Kumar, S.; Rosenberg, J. M.; Bouzida, D.; Swendsen, R. H.; Kollman, P. A. THE weighted histogram analysis method for free-energy calculations on biomolecules. I. The method. *Journal of Computational Chemistry* **1992**, *13*, 1011–1021.

(57) Wolynes, P. G.; Onuchic, J. N.; Thirumalai, D. Navigating the folding routes. *Science* **1995**, *267*, 1619–1620.

(58) Chu, X.; Gan, L.; Wang, E.; Wang, J. Quantifying the topography of the intrinsic energy landscape of flexible biomolecular recognition. *Proceedings of the National Academy of Sciences* **2013**, *110*, E2342–E2351.

(59) Freitas, F. C.; Ferreira, P. H. B.; Favaro, D. C.; Oliveira, R. J. d. Shedding light on the inhibitory mechanisms of SARS-CoV-1/CoV-2 spike proteins by ACE2-designed peptides. *Journal of chemical information and modeling* **2021**, *61*, 1226–1243.

(60) Tamiola, K.; Acar, B.; Mulder, F. A. Sequence-specific random coil chemical shifts of intrinsically disordered proteins. *Journal of the American Chemical Society* **2010**, *132*, 18000–18003.

(61) Shen, Y.; Bax, A. SPARTA+: A modest improvement in empirical NMR chemical shift prediction by means of an artificial neural network. *Journal of Biomolecular NMR* **2010**, *48*, 13–22.

(62) Vranken, W. F.; Boucher, W.; Stevens, T. J.; Fogh, R. H.; Pajon, A.; Llinas, M.; Ulrich, E. L.; Markley, J. L.; Ionides, J.; Laue, E. D. The CCPN data model for NMR spectroscopy: Development of a software pipeline. *Proteins: Structure, Function, and Bioinformatics* **2005**, *59*, 687–696.

(63) Delaglio, F.; Grzesiek, S.; Vuister, G. W.; Zhu, G.; Pfeifer, J.; Bax, A. NMRPipe: A multidimensional spectral processing system based on UNIX pipes. *Journal of Biomolecular NMR* **1995**, *6*, 277–293.

(64) Cardoso, M. V.; Rivera, J. D.; Vitale, P. A.; Degenhardt, M. F.; Abiko, L. A.; Oliveira, C. L.; Salinas, R. K. CALX-CBD1 Ca2+-Binding Cooperativity Studied by NMR Spectroscopy and ITC with Bayesian Statistics. *Biophysical Journal* **2020**, *119*, 337–348.

(65) Farrow, N. A.; Zhang, O.; Forman-Kay, J. D.; Kay, L. E. A heteronuclear correlation experiment for simultaneous determination of 15 N longitudinal decay and chemical exchange rates of systems in slow equilibrium. *Journal of biomolecular NMR* **1994**, *4*, 727–734.

(66) Whitmore, L.; Wallace, B. A. DICHROWEB, an online server for protein secondary structure analyses from circular dichroism spectroscopic data. *Nucleic Acids Research* **2004**, *32*, 668–673.

(67) Whitmore, L.; Wallace, B. A. Protein secondary structure analyses from circular dichroism spectroscopy: Methods and reference databases. *Biopolymers* **2008**, *89*, 392–400.

(68) Sjöstrand, L. Method Development for Thermal Stability Analysis by Circular Dichroism: Application to the Abp1p SH3 domain from yeast. 2018.

(69) Greenfield, N. J. Using circular dichroism collected as a function of temperature to determine the thermodynamics of protein unfolding and binding interactions. *Nature Protocols* **2007**, *1*, 2527–2535.

(70) Seelig, J.; Schönfeld, H.-J. Thermal protein unfolding by differential scanning calorimetry and circular dichroism spectroscopy: Two-state model versus sequential unfolding . *Quarterly Reviews of Biophysics* **2016**, *49*.

(71) Nakatani, H.; Haga, M.; Hiromi, K. Kinetic studies on binding of bovine serum albumin with 1-anilino-8-naphthalene sulfonate. *FEBS Letters* **1974**, *43*, 293–296.

(72) Yu, L.; Li, D.-W.; Brüschweiler, R. Balanced Amino-Acid-Specific Molecular Dynamics Force Field for the Realistic Simulation of Both Folded and Disordered Proteins. *Journal of Chemical Theory and Computation* **2020**, *16*, 1311–1318.

(73) Van Der Spoel, D.; Lindahl, E.; Hess, B.; Groenhof, G.; Mark, A. E.; Berendsen, H. J. C. GROMACS: Fast, flexible, and free. *Journal of Computational Chemistry* **2005**, *26*, 1701–1718.

(74) Søndergaard, C. R.; Olsson, M. H.; Rostkowski, M.; Jensen, J. H. Improved treatment of ligands and coupling effects in empirical calculation and rationalization of p K a values. *Journal of chemical theory and computation* **2011**, *7*, 2284–2295.

(75) Whitford, P. C.; Noel, J. K.; Gosavi, S.; Schug, A.; Sanbonmatsu, K. Y.; Onuchic, J. N. An all-atom structure-based potential for proteins: Bridging minimal models with all-atom empirical forcefields. *Proteins: Structure, Function, and Bioinformatics* **2009**, *75*, 430–441.

(76) Taketomi, H.; Ueda, Y.; Gō, N. Studies on protein folding, unfolding and fluctuations by computer simulation: The effect of specific amino acid sequence represented by specific inter-unit interactions. *International journal of peptide and protein research* **1975**, *7*, 445–459.

(77) Clementi, C.; Nymeyer, H.; Onuchic, J. N. Topological and energetic factors: What determines the structural details of the transition state ensemble and 'en-route' intermediates for protein folding? An investigation for small globular proteins. *Journal of Molecular Biology* **2000**, *298*, 937–953.

(78) Wang, J.; Oliveira, R. J.; Chu, X.; Whitford, P. C.; Chahine, J.; Han, W.; Wang, E.; Onuchic, J. N.; Leite, V. B. Topography of funneled landscapes determines the ther-

modynamics and kinetics of protein folding. *Proceedings of the National Academy of Sciences* **2012**, *109*, 15763–15768.

(79) Sutto, L.; Lätzer, J.; Hegler, J. A.; Ferreiro, D. U.; Wolynes, P. G. Consequences of localized frustration for the folding mechanism of the IM7 protein. *Proceedings of the National Academy of Sciences* **2007**, *104*, 19825–19830.

(80) Contessoto, V. G.; Lima, D. T.; Oliveira, R. J.; Bruni, A. T.; Chahine, J.; Leite, V. B. Analyzing the effect of homogeneous frustration in protein folding. *Proteins: Structure, Function, and Bioinformatics* **2013**, *81*, 1727–1737.

(81) Ferreira, P. H. B.; Freitas, F. C.; McCully, M. E.; Slade, G. G.; de Oliveira, R. J. The role of electrostatics and folding kinetics on the thermostability of homologous cold shock proteins. *Journal of chemical information and modeling* **2020**, *60*, 546–561.

(82) Noel, J. K.; Levi, M.; Raghunathan, M.; Lammert, H.; Hayes, R. L.; Onuchic, J. N.; Whitford, P. C. SMOG 2: A Versatile Software Package for Generating Structure-Based Models. *PLOS Computational Biology* **2016**, *12*, 1–14.

(83) Ferrenberg, A. M.; Swendsen, R. H. New Monte Carlo Technique for Studying Phase Transitions. *Physical review letters* **1988**, *61*, 2635–2638.

(84) Freitas, F. C.; Maldonado, M.; Oliveira Junior, A. B.; Onuchic, J. N.; Oliveira, R. J. d. Biotin-painted proteins have thermodynamic stability switched by kinetic folding routes. *The Journal of Chemical Physics* **2022**, *156*, 195101.

(85) Humphrey, W.; Dalke, A.; Schulten, K. VMD: visual molecular dynamics. *Journal of molecular graphics* **1996**, *14*, 33–38.

(86) Pettersen, E. F.; Goddard, T. D.; Huang, C. C.; Couch, G. S.; Greenblatt, D. M.; Meng, E. C.; Ferrin, T. E. UCSF Chimera—A visualization system for exploratory research and analysis. *Journal of Computational Chemistry* **2004**, *25*, 1605–1612.

(87) Hunter, J. D. Matplotlib: A 2D graphics environment. *Computing in science & engineering* **2007**, *9*, 90–95.

TOC Graphic